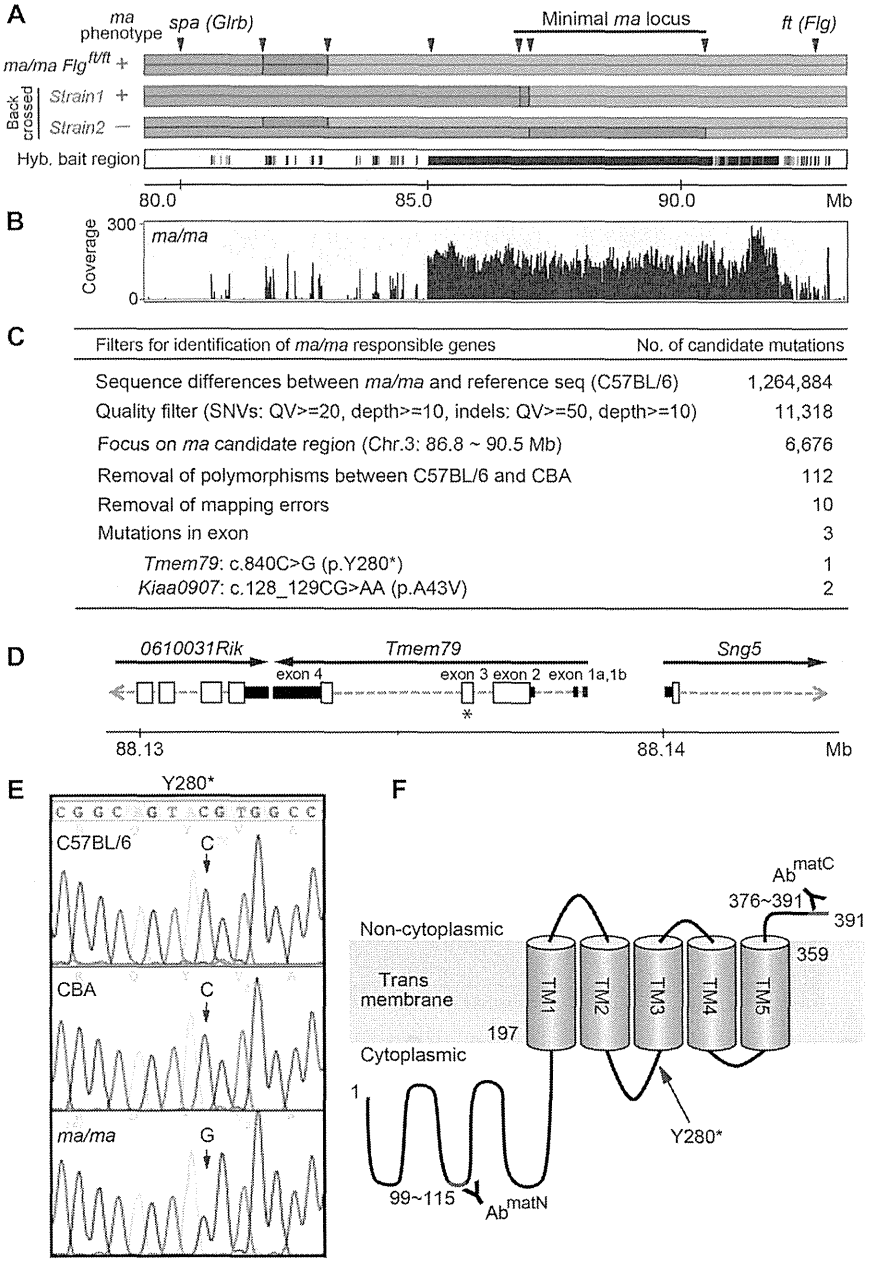

FIG 2. Identification of the *Tmem79* mutation as the gene responsible for *ma*. **A,** The minimal *ma* locus was defined by backcrossing *ma/ma* mice with C57BL/6 mice. The *2 rectangles* indicate the mouse alleles. *ma/ma Flg*$^{ft/ft}$, Original flaky tail mouse; *ma (+/−)*, matted positive or negative mice; *blue*, C57BL/6 allele; *pink*, CBA allele; *gray*, indistinguishable region. *Triangles* indicate the positions of polymorphic markers in C57BL/6 and CBA. *Hyb. bait regions* are the hybridization bait regions for targeted resequencing. **B,** Sequence coverage of the *ma* candidate region with targeted resequencing. **C,** Identification of the *ma* gene and a number of additional candidates carrying variations identified by means of targeted resequencing. **D,** Genomic structure of *Tmem79*. The *asterisk* in exon 3 indicates the c.840C>G mutation. *White* and *black boxes* indicate coding and noncoding regions, respectively. **E,** Confirmation of the *Tmem79* mutation in *ma/ma* mice by means of Sanger sequencing. **F,** Predicted protein structure of Tmem79. The location of transmembrane domains and topology were predicted by using the programs SOSUI and Octopus. Two rabbit anti-Tmem79 antibodies (Ab^{matN} and Ab^{matC}) were raised against synthetic peptides derived from amino acids 99 to 115 and 376 to 391, respectively. p.Y280* is located between the second and third transmembrane domains of the Tmem79 protein.

Therefore we defined a minimal *ma* locus by backcrossing *ma/ma* mice with WT mice and applied target enrichment, followed by next-generation DNA sequencing (Fig 2, *A-C*). After filtering sequence differences and making a detailed comparison of *ma/ma* and reference genome sequences, we found 3 nucleotide substitutions in the exon of *ma/ma* mice: c.840C>G in *Tmem79* (nonsense mutation p.Y280*; Fig 2, *C* and *E*) and a 2-base substitution in *Kiaa0907*, c.128_129CG>TT (missense mutation p.A43V;

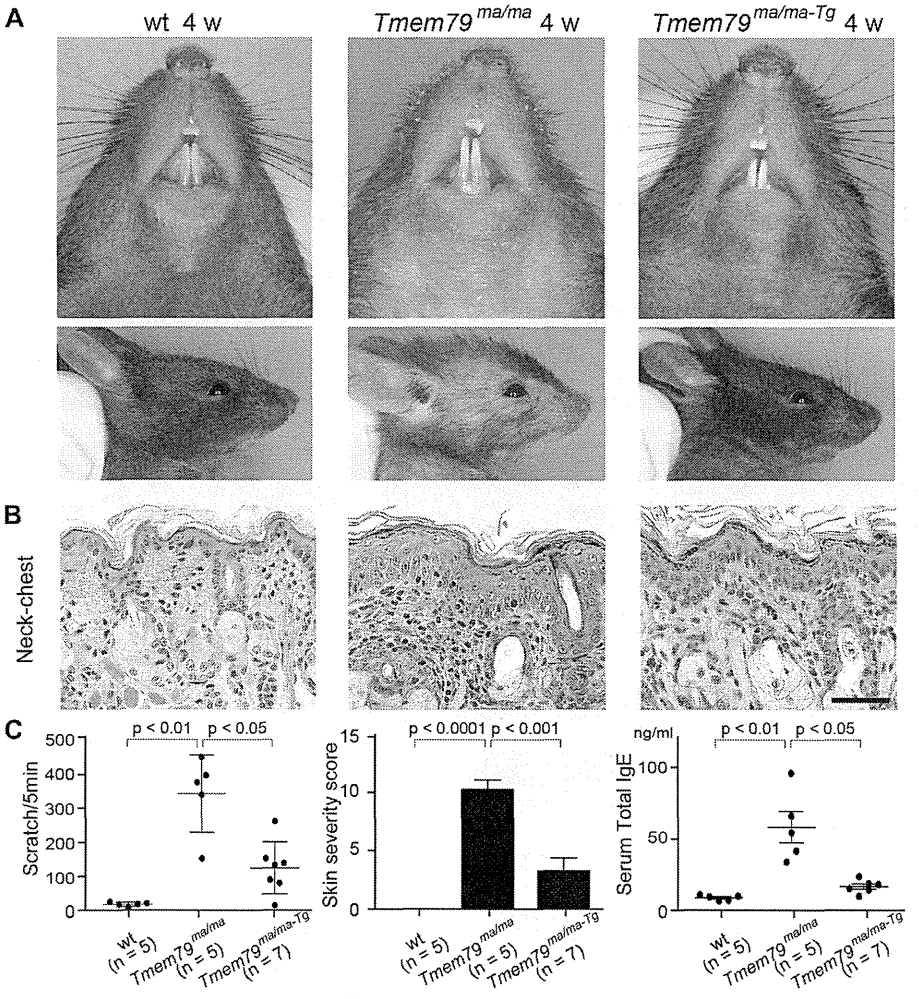

FIG 3. Rescue of the *ma* phenotype in *Tmem79*$^{ma/ma}$ mice by means of transgenic reintroduction of WT *Tmem79*. **A,** Gross dermatitis phenotype of 4-week-old WT (C57BL/6), *Tmem79*$^{ma/ma}$, and *Tmem79*$^{ma/ma\text{-}Tg}$ mice. **B,** Histology of the skin on the neck-chest. *Bars* = 100 μm. **C,** Scratching frequency, skin severity score, and serum total IgE level were compared among 4-week-old WT (C57BL/6, n = 5), *Tmem79*$^{ma/ma}$ (n = 5), and *Tmem79*$^{ma/ma\text{-}Tg}$ (n = 7) mice.

Fig 2, *C*). Because *Tmem79* carried a nonsense mutation and was predominantly expressed in the skin of WT mice (see Fig E2, *A* and *B*, in this article's Online Repository at www.jacionline.org), we focused on further characterization of *Tmem79*. The *Tmem79* gene was composed of 5 exons that encode a 43.4-kDa protein with 5 transmembrane domains (exon 1a and exon 1b for spliced variant). The Tmem79 protein N-terminus is located in the cytoplasm, as predicted by transmembrane prediction programs. The c.840C>G mutation is located in exon 3, and p.Y280* is located between the second and third transmembrane domains (Fig 2, *F*).

Transgenic rescue of the matted hair and dermatitis phenotype of *Tmem79*$^{ma/ma}$ mice

To confirm that *Tmem79* was responsible for the *matted* hair phenotype and spontaneous dermatitis in *Tmem79*$^{ma/ma}$ mice, we attempted to rescue the phenotype by introducing a WT *Tmem79* transgene under control of the *Tmem79* promoter. We subcloned a fragment containing the entire *Tmem79* genomic locus, including the *Tmem79* promoter region from bacterial artificial chromosome clone RP23-168E1, into pUC118 and used this for pronuclear injection of the *Tmem79* transgene (see Fig E1). The resultant *Tmem79*^{Tg} mice were subsequently mated with *Tmem79*$^{ma/ma}$ mice. These *Tmem79*$^{ma/ma\text{-}Tg}$ mice no longer developed matted hair or spontaneous dermatitis at 4 weeks, when the phenotype became apparent in *Tmem79*$^{ma/ma}$ mice (Fig 3, *A* and *B*). *Tmem79*$^{ma/ma\text{-}Tg}$ mice also displayed significantly less frequent scratching behavior than *Tmem79*$^{ma/ma}$ mice (Fig 3, *C*). The skin severity scores and serum total IgE levels of *Tmem79*$^{ma/ma\text{-}Tg}$ mice were significantly lower than those of *Tmem79*$^{ma/ma}$ mice. *Tmem79*$^{ma/ma\text{-}Tg}$ mice remained free from any apparent dermatitis phenotype for as long as 1 year. These findings confirm that *Tmem79* was responsible for the matted hair and dermatitis phenotype observed in *Tmem79*$^{ma/ma}$ mice.

Tmem79 is primarily expressed in the outermost cells of the stratum granulosum

After examining various organs, *Tmem79* mRNA was expressed most strongly in the epidermis (see Fig E2). Rabbit antibodies raised against the synthesized peptides containing N-terminal

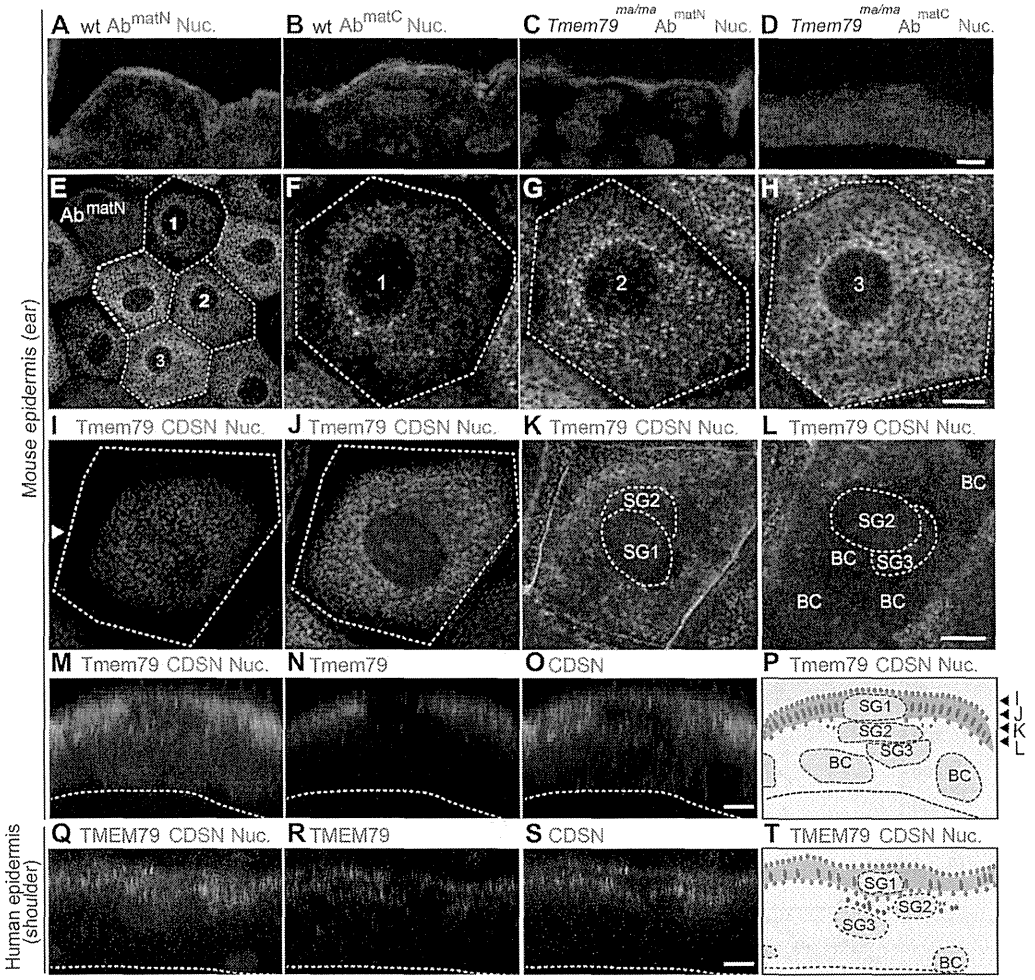

FIG 4. *Localization of Tmem79 in the epidermis.* **A-D,** *Vertical skin sections were immunostained with* Ab^{matN} *and* Ab^{matC} *for WT (C57BL/6) and* $Tmem79^{ma/ma}$ *mice. Red,* Tmem79; *blue,* nucleus. **E-H,** Horizontal confocal images of Tmem79 stained with Ab^{matN} in SG1 cells of the mouse epidermal sheet. *Dotted lines* indicate the boundary of the SG1 cells, and the numbers *(1-3)* in the centers of the cells indicate the cell location in Fig 4, *E.* **I-L,** *Z-axis scanning confocal images of Tmem79* (Ab^{matN}) *and CDSN in the layers of* the mouse epidermal sheet. *Red,* Tmem79; *green,* CDSN; *blue,* nucleus. *Dotted lines* indicate the boundary of the SG1 cells (Fig 4, *I* and *J*) and nucleus (Fig 4, *K* and *L*). *BC,* Basal cell. The *triangle* in Fig 4, *I,* indicates the position of the reconstituted vertical image in Fig 4, *M.* See also Video E1. **M-O,** Reconstituted vertical images from the *z*-axis scanning confocal images from Fig 4, *I* to *L.* The *dotted line* indicates the position of the basement membrane zone. See also Video E2. **P,** The scheme for the reconstituted vertical images of the mouse epidermal sheet. The positions of the *triangles* indicate the levels of each confocal horizontal image (Fig 4, *I-L*). **Q-S,** The reconstituted vertical images of Tmem79 (Ab^{matN}) and CDSN from z-axis scanning confocal images of the human epidermal sheet. *Red,* Tmem79; *green,* CDSN; *blue,* nucleus. **T,** Scheme of the reconstituted vertical images of the human epidermal sheet. *Bars* = 5 μm.

residues 99 to 115 (Ab^{matN}) and C-terminal residues 376 to 391 (Ab^{matC}) of Tmem79 stained the outermost layer of the stratum granulosum (SG) cells (SG1 cells) of WT mice, whereas Ab^{matN} staining, but not Ab^{matC} staining, was observed in vertical epidermal sections from $Tmem79^{ma/ma}$ mice (Fig 4, *A-D*), indicating that the truncated Tmem79 is expressed in $Tmem79^{ma/ma}$ mice. Because SG cells, which differentiate to form the SC, are largely flattened and piled up at different stages of differentiation, whole-mount staining of epidermal sheets was used to examine the expression pattern in SG1 cells.[26] When the epidermal sheet *en face* views were examined by using confocal microscopy, the Tmem79 staining showed a dot-like, tubular, or reticular pattern depending on the maturation stage of SG1 cell differentiation during SC biogenesis (Fig 4, *E-H*). Costaining with corneodesmosin (CDSN), which labeled SG1 cell membranes, revealed that Tmem79 was exclusively expressed in the cytoplasm of SG1 cells in mice, as seen in vertically reconstituted images (Fig 4, *I-P*; see Videos E1 and E2 in this article's Online Repository at www.jacionline.org). Similarly, human TMEM79 was primarily detected in the cytoplasm of SG1 cells and was detected in SG2 cells to a lesser degree (Fig 4, *Q-T*), suggesting that the function of Tmem79 is conserved between mice and humans.

Colocalization of Tmem79 and TGN marker in SG1 cells

Tmem79 was costained with antibodies for various organelle markers to further characterize the intracellular localization of

Tmem79 in SG1 cells (Fig 5, *A-D*). Tmem79 most closely colocalized with TGN46, a marker of the TGN.[28] LAMP1, a marker for lysosomes, tended to costain at the apical tips of Tmem79-positive organelles.[29] Tmem79 did not colocalize with GM130 (*cis*-Golgi network), EEA1 (early endosome), SNAP29 (vesicle transport), or CDSN (CDSN and LG).[30-33] Immunoelectron microscopy confirmed that Tmem79 and TGN46 were colocalized in human epidermal SG1 and SG2 cells (Fig 5, *E*).[30-33]

Reduced expression of LG-secreted proteins in *Tmem79*$^{ma/ma}$ mice

The TGN plays a central role in protein sorting among the organelles of the secretory pathway.[34,35] The LG secretory system specializes in the polarized secretion of various proteases, protease inhibitors, and lipids in the SG layers to form the SC.[36] Therefore we examined LG-secreted proteins in *Tmem79*$^{ma/ma}$ mice to examine whether Tmem79 is involved in the LG secretory system (Fig 6). Although there were no obvious changes in the vertical section staining for FLG and LOR or whole-mount staining for TGN46 and Tmem79 N-terminal, both vertical sections and whole-mount staining for LG-secreted proteins (KLK5 and LEKTI) was significantly reduced in *Tmem79*$^{ma/ma}$ mice compared with WT mice (Fig 6, *A-C*). In contrast, this reduced staining was remarkably rescued in *Tmem79*$^{ma/ma\text{-}Tg}$ mice (Fig 6, *D*). These results suggest that *Tmem79* is involved in the LG secretory system and that *Tmem79* deficiency directly or indirectly causes dysfunction of this system.

Impaired SC formation in *Tmem79*$^{ma/ma}$ mice

Next we examined SC formation in *Tmem79*$^{ma/ma}$ mice. Although there were no apparent structural changes to the SC layers on safranin staining, physical stress caused by tape stripping resulted in quite different peeling patterns of the SC layers in WT and *Tmem79*$^{ma/ma}$ mice (Fig 7, *A* and *B*). Although the SC layers of WT mice peeled off evenly and the amount of desquamated SC decreased with the number of strippings, the SC layers of *Tmem79*$^{ma/ma}$ mice peeled off unevenly as blocks, and the entire SC layer was focally removed after 10 tape-stripping applications. The number of regions in which tape stripping removed the entire SC layer was significantly greater in *Tmem79*$^{ma/ma}$ mice than in WT mice (Fig 7, *C*). These findings indicate that *Tmem79*$^{ma/ma}$ mice have impaired SC formation with less resistance to physical external stress.

DISCUSSION

Original double-mutant flaky tail (*ma/ma Flg*$^{ft/ft}$) mice express truncated profilaggrin and significantly reduced mature filaggrin, show enhanced TEWL and decreased SC hydration, and develop spontaneous dermatitis with increased IgE levels.[13,14] Thus *Tmem79*$^{ma/ma}$ *Flg*$^{ft/ft}$ mice have been widely used as a mouse model of AD with filaggrin deficiency. However, genetically engineered *Flg*$^{-/-}$ mice had no apparent change in TEWL or SC hydration compared with WT mice and did not develop dermatitis under SPF conditions, although filaggrin was completely absent.[8] The onset of dermatitis in *Flg*$^{-/-}$ mice under conventional conditions remains to be determined. This conflicting observation between flaky tail mice and *Flg*$^{-/-}$ mice led us to investigate the gene responsible for the *ma* phenotype. We identified a nonsense mutation (c.840C>G, p.Y280*) in the *Tmem79* gene. *Tmem79*$^{ma/ma}$ mice without the filaggrin mutation have enhanced TEWL and decreased SC hydration and develop spontaneous dermatitis with increased IgE levels. Mutations of both the *Flg* and *Tmem79* genes result in altered SC formation and impaired SC barrier, although in different pathways. Therefore all of the previous work with the double-mutant flaky tail mice in the context of filaggrin deficiency needs to be carefully re-evaluated.[15-19,37] The contribution of the *Tmem79* mutation has to be reconsidered in those studies.

Several skin barrier–related genes responsible for SC formation have already been isolated, and *Tmem79* is a new member in that category. Defects in these skin barrier–related genes often

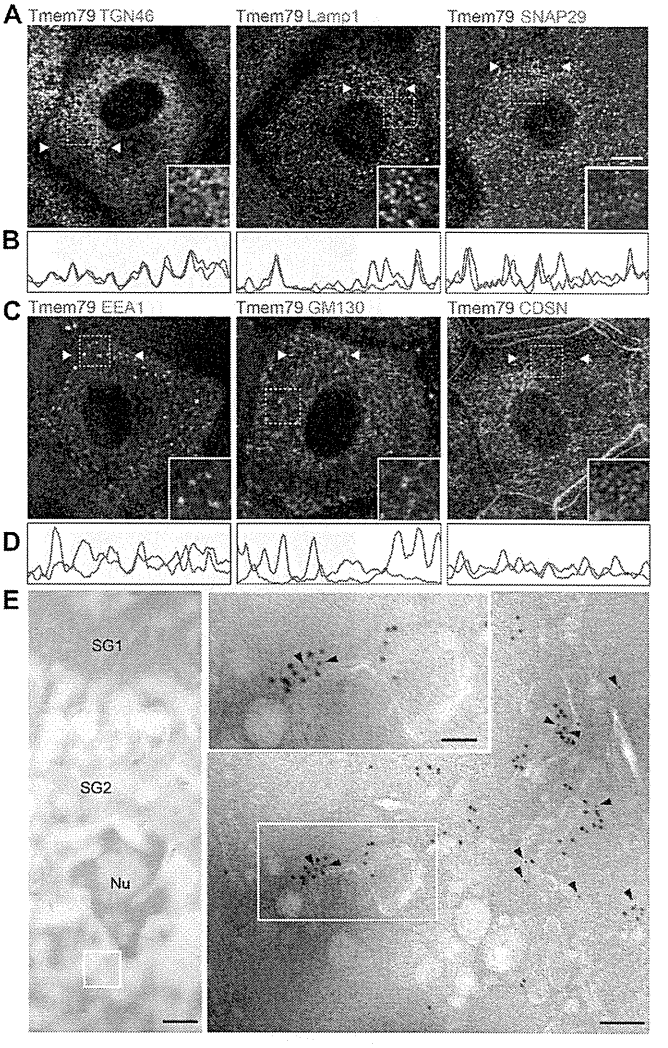

FIG 5. Costaining of Tmem79 with intracellular organelle markers in SG1 cells. **A** and **C,** Horizontal confocal images of coimmunostaining with Tmem79 (Ab^{matN}; *red*) and various intracellular organelle markers *(green),* including TGN46 (*trans*-Golgi network), LAMP1 (lysosomes), SNAP29 (vesicle transport), EEA1 (early endosomes), GM130 (*cis*-Golgi), and CDSN (corneodesmosome and LG). *Insets* are magnified images of the indicated areas *(dotted squares). Bars* = 5 μm. **B** and **D,** Colocalization analysis of multicolor confocal immunostaining. Each *color curve* indicates the relative intensity of the immunostaining for each protein (*red,* Tmem79; *green,* each organelle marker) between the *2 triangles* in each image. **E,** Immunoelectron microscopic image of colocalized Tmem79 and TGN46 in human skin. The *square in the left column* is enlarged in the *right column.* The *rectangle in the right column* is enlarged in the *upper left corner.* Tmem79, *arrowheads,* 5 nm gold; TGN46, 10 nm gold. *Nu,* Nucleus. *Bars* = 1 μm *(left),* 100 nm *(right),* and 50 nm *(center).*

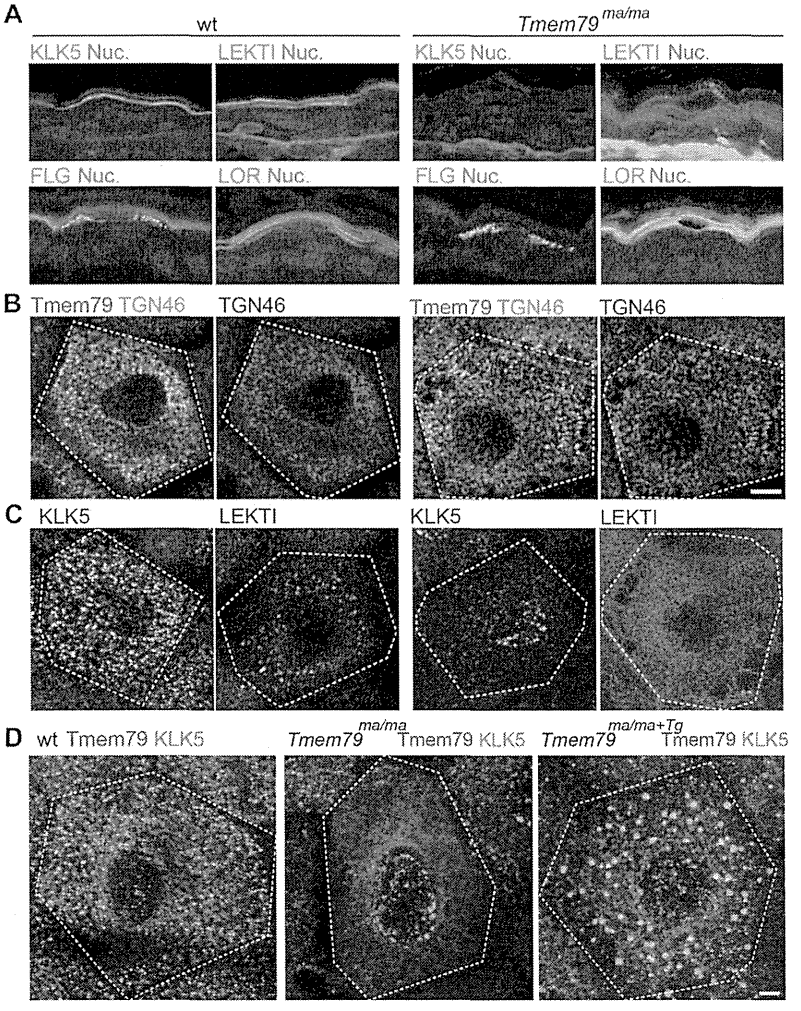

FIG 6. LG secretory system dysfunction in *Tmem79*$^{ma/ma}$ mice. **A,** Vertical skin sections were immunostained with KLK5, LEKTI, FLG, and LOR in WT (C57BL/6) and *Tmem79*$^{ma/ma}$ mice. *Green,* each protein; *blue,* nucleus. **B,** Horizontal confocal images of Tmem79 and TGN46 in the SG1 cells of the mouse epidermal sheet in WT (C57BL/6) and *Tmem79*$^{ma/ma}$ mice. *Red,* Tmem79 (Ab^{matN}); *green,* TGN46. *Dotted lines* indicate the boundary of the SG1 cells. *Bars* = 5 μm. **C,** Horizontal confocal images of the LG secretory proteins (KLK5 and LEKTI) in SG1 cells of the mouse epidermal sheet in WT (C57BL/6) and *Tmem79*$^{ma/ma}$ mice. *Dotted lines* indicate the boundary of the SG1 cells. *Bars* = 5 μm. **D,** Horizontal confocal images of Tmem79 (Ab^{matN}) and KLK5 proteins in the SG1 cells of the mouse epidermal sheets from 8-week-old (C57BL/6), *Tmem79*$^{ma/ma}$, and *Tmem79*$^{ma/ma\text{-}Tg}$ mice. *Red,* Tmem79; *green,* KLK5. *Bars* = 5 μm.

result in skin disorders in humans. *CDSN* encodes a component of CDSN that plays the role of an adhesion molecule for corneocytes, and *CDSN* defects cause peeling skin syndrome, in which patients have ichthyosiform erythroderma with superficial exfoliation.[38] *ST14* encodes the protease matriptase, and *ST14* defects cause ichthyosis with hypotrichosis syndrome.[39] *SPINK5* encodes the protease inhibitor LEKTI, and *SPINK5* defects cause Netherton syndrome, which is characterized by congenital ichthyosiform erythroderma with bamboo hair formation.[40] *ABCA12* encodes a lipid transporter, and *ABCA12* defects cause both autosomal recessive congenital ichthyosis 4A (ARCI4A) and Harlequin ichthyosis.[41,42] SNAP29 encodes a SNARE protein involved in intracellular trafficking, and *SNAP29* mutations cause cerebral dysgenesis, neuropathy, ichthyosis, and keratoderma (CEDNIK) syndrome. Among those skin disorder–related genes, several are linked to the LG secretory system, which plays an essential role in intact SC formation and maturation. CDSN and LEKTI are secreted through the LG, ABCA12 is localized in the LG and functions as a lipid transporter, and SNAP29 is member of the t-SNARE proteins that are associated with granule fusion to the cell membrane in the LG secretory system.[43] *Tmem79* is a novel skin barrier–related gene involved in the LG secretory system, and *Tmem79* deficiency causes abnormal secretion of several secreted proteins, which results in impaired SC barrier formation and spontaneous dermatitis in mice. The involvement of *Tmem79* in any human skin disorder remains to be determined.

Tmem79$^{ma/ma}$ *Flg*$^{ft/ft}$ and *Tmem79*$^{ma/ma}$ mice also display the matted hair phenotype, which was originally described as (1) erection of hair, (2) matted clumps of hair (hair with a tendency to stick together), (3) a tendency to baldness, and (4) change in hair color.[11] The hair phenotype was rescued by introducing with WT *Tmem79* transgene, therefore, *Tmem79*$^{ma/ma}$ was also responsible for the hair phenotype. Because *Tmem79*$^{ma/ma}$ mice

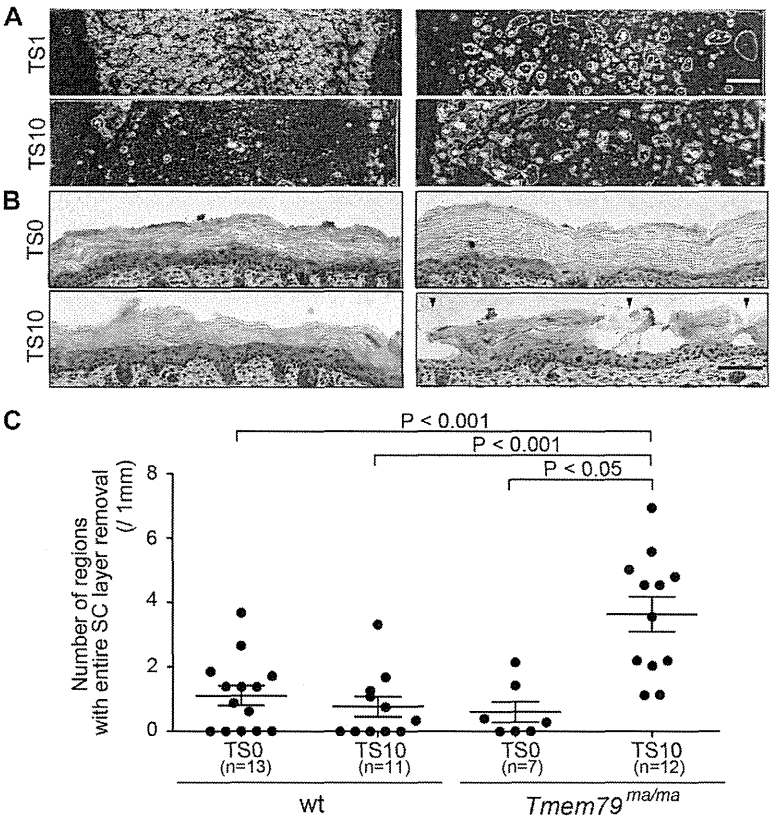

FIG 7. Impaired SC formation in *Tmem79*$^{ma/ma}$ *mice.* **A,** The SC layers that came off with the tape after tape stripping are shown for 5-day-old WT (C57BL/6) and *Tmem79*$^{ma/ma}$ mice. *TS1,* First tape stripping; *TS10,* 10th tape stripping. *Bars* = 2 mm. **B,** The SC layers were visualized by means of safranin staining before *(TS0)* and after *(TS10)* tape stripping of 5-day-old WT and *Tmem79*$^{ma/ma}$ mice. *Triangles* indicate regions with entire SC layer removal. *Bars* = 100 μm. **C,** The number of regions with removal of the entire SC layer per 1 mm was counted and compared between WT and *Tmem79*$^{ma/ma}$ mice before (*TS0*; WT mice, n = 13, *Tmem79*$^{ma/ma}$ mice, n = 7) and after (*TS10*; WT mice, n = 11; *Tmem79*$^{ma/ma}$ mice, n = 12) tape stripping.

have moist and oily hair, we suspected that matted clump formation might be due to differences in lipid composition of the surface of the hair. This hypothesis was indeed true; lipid composition analysis revealed more cholesterol ester members in the hair of *Tmem79*$^{ma/ma}$ *Flg*$^{ft/ft}$ mice than in WT mice (data not shown). This difference is likely due to an impaired LG secretory system in the hair follicles. Further investigation is necessary to understand how *Tmem79*$^{ma/ma}$ induces the matted hair phenotype.

Although we identified *Tmem79*$^{ma/ma}$ as the gene responsible for spontaneous dermatitis in double-mutant flaky tail mice and matted mice, the exact mechanisms involved in the onset of dermatitis remain to be elucidated. What is the exact molecular role of Tmem79 in the LG secretory system? How does the impaired LG secretory system affect SC formation? Why do impaired SC barriers result in spontaneous dermatitis? Are any commensal bacteria involved in this process? Although many questions remain to be answered to fully understand the pathophysiologic mechanism of dermatitis caused by *Tmem79*$^{ma/ma}$ deficiency, the identification of *Tmem79* as a novel skin barrier–related gene will open a new path to dissect the fundamental mechanisms of SC barrier formation and provide a new target for the development of therapeutic strategies for atopic diseases.

We thank Ms Ikuko Koya and members of the Collaborative Research Resources, Keio University School of Medicine, for their excellent technical assistance and Ms Mariko Okajima for her excellent secretarial help on this project.

Clinical implications: *Tmem79* is a novel skin barrier–related gene involved in the pathogenesis of dermatitis, and matted mice or *Tmem79*-deficient mice provide a valuable tool for dissecting pathophysiologic mechanisms of skin barrier disruption and AD.

REFERENCES

1. Palmer CN, Irvine AD, Terron-Kwiatkowski A, Zhao Y, Liao H, Lee SP, et al. Common loss-of-function variants of the epidermal barrier protein filaggrin are a major predisposing factor for atopic dermatitis. Nat Genet 2006;38:441-6.
2. Smith FJ, Irvine AD, Terron-Kwiatkowski A, Sandilands A, Campbell LE, Zhao Y, et al. Loss-of-function mutations in the gene encoding filaggrin cause ichthyosis vulgaris. Nat Genet 2006;38:337-42.
3. Spergel JM. From atopic dermatitis to asthma: the atopic march. Ann Allergy Asthma Immunol 2010;105:99-109, 17.
4. McAleer MA, Irvine AD. The Multifunctional role of filaggrin in allergic skin disease. J Allergy Clin Immunol 2013;131:280-91.
5. Weidinger S, O'Sullivan M, Illig T, Baurecht H, Depner M, Rodriguez E, et al. Filaggrin mutations, atopic eczema, hay fever, and asthma in children. J Allergy Clin Immunol 2008;121:1203-9.e1.
6. Brown SJ, Asai Y, Cordell HJ, Campbell LE, Zhao Y, Liao H, et al. Loss-of-function variants in the filaggrin gene are a significant risk factor for peanut allergy. J Allergy Clin Immunol 2011;127:661-7.
7. Sandilands A, Sutherland C, Irvine AD, McLean WH. Filaggrin in the frontline: role in skin barrier function and disease. J Cell Sci 2009;122:1285-94.

8. Kawasaki H, Nagao K, Kubo A, Hata T, Shimizu A, Mizuno H, et al. Altered stratum corneum barrier and enhanced percutaneous immune responses in filaggrin-null mice. J Allergy Clin Immunol 2012;129:1538-46.e6.
9. Kubo A, Nagao K, Amagai M. Epidermal barrier dysfunction and cutaneous sensitization in atopic diseases. J Clin Invest 2012;122:440-7.
10. Henderson J, Northstone K, Lee SP, Liao H, Zhao Y, Pembrey M, et al. The burden of disease associated with filaggrin mutations: a population-based, longitudinal birth cohort study. J Allergy Clin Immunol 2008;121:872-7.e9.
11. Searle AG, Spearman RI. 'Matted', a new hair-mutant in the house-mouse: genetics and morphology. J Embryol Exp Morphol 1957;5:93-102.
12. Lane PW. Two new mutations in linkage group XVI of the house mouse. Flaky tail and varitint-waddler-J. J Hered 1972;63:135-40.
13. Presland RB, Boggess D, Lewis SP, Hull C, Fleckman P, Sundberg JP. Loss of normal profilaggrin and filaggrin in flaky tail (ft/ft) mice: an animal model for the filaggrin-deficient skin disease ichthyosis vulgaris. J Invest Dermatol 2000;115:1072-81.
14. Fallon PG, Sasaki T, Sandilands A, Campbell LE, Saunders SP, Mangan NE, et al. A homozygous frameshift mutation in the mouse Flg gene facilitates enhanced percutaneous allergen priming. Nat Genet 2009;41:602-8.
15. Moniaga CS, Kabashima K. Filaggrin in atopic dermatitis: flaky tail mice as a novel model for developing drug targets in atopic dermatitis. Inflamm Allergy Drug Targets 2011;10:477-85.
16. Moniaga CS, Egawa G, Kawasaki H, Hara-Chikuma M, Honda T, Tanizaki H, et al. Flaky tail mouse denotes human atopic dermatitis in the steady state and by topical application with *Dermatophagoides pteronyssinus* extract. Am J Pathol 2010;176:2385-93.
17. Oyoshi MK, Murphy GF, Geha RS. Filaggrin-deficient mice exhibit TH17-dominated skin inflammation and permissiveness to epicutaneous sensitization with protein antigen. J Allergy Clin Immunol 2009;124:485-93.e1.
18. Scharschmidt TC, Man MQ, Hatano Y, Crumrine D, Gunathilake R, Sundberg JP, et al. Filaggrin deficiency confers a paracellular barrier abnormality that reduces inflammatory thresholds to irritants and haptens. J Allergy Clin Immunol 2009;124:496-506, e1-6.
19. Kezic S, O'Regan GM, Lutter R, Jakasa I, Koster ES, Saunders S, et al. Filaggrin loss-of-function mutations are associated with enhanced expression of IL-1 cytokines in the stratum corneum of patients with atopic dermatitis and in a murine model of filaggrin deficiency. J Allergy Clin Immunol 2012;129:1031-3.e1.
20. Nakai K, Yoneda K, Hosokawa Y, Moritue T, Presland RB, Fallon PG, et al. Reduced expression of epidermal growth factor receptor, e-cadherin, and occludin in the skin of flaky tail mice is due to filaggrin and loricrin deficiencies. Am J Pathol 2012;181:969-77.
21. Li H, Durbin R. Fast and accurate long-read alignment with Burrows-Wheeler transform. Bioinformatics 2010;26:589-95.
22. Li H, Handsaker B, Wysoker A, Fennell T, Ruan J, Homer N, et al. The Sequence Alignment/Map format and SAMtools. Bioinformatics 2009;25:2078-9.
23. Hirokawa T, Boon-Chieng S, Mitaku S. SOSUI: classification and secondary structure prediction system for membrane proteins. Bioinformatics 1998;14:378-9.
24. Viklund H, Elofsson A. OCTOPUS: improving topology prediction by two-track ANN-based preference scores and an extended topological grammar. Bioinformatics 2008;24:1662-8.
25. Leung DY, Hirsch RL, Schneider L, Moody C, Takaoka R, Li SH, et al. Thymopentin therapy reduces the clinical severity of atopic dermatitis. J Allergy Clin Immunol 1990;85:927-33.
26. Kubo A, Nagao K, Yokouchi M, Sasaki H, Amagai M. External antigen uptake by Langerhans cells with reorganization of epidermal tight junction barriers. J Exp Med 2009;206:2937-46.
27. Ishida-Yamamoto A, Simon M, Kishibe M, Miyauchi Y, Takahashi H, Yoshida S, et al. Epidermal lamellar granules transport different cargoes as distinct aggregates. J Invest Dermatol 2004;122:1137-44.
28. Kain R, Angata K, Kerjaschki D, Fukuda M. Molecular cloning and expression of a novel human trans-Golgi network glycoprotein, TGN51, that contains multiple tyrosine-containing motifs. J Biol Chem 1998;273:981-8.
29. Mane SM, Marzella L, Bainton DF, Holt VK, Cha Y, Hildreth JE, et al. Purification and characterization of human lysosomal membrane glycoproteins. Arch Biochem Biophys 1989;268:360-78.
30. Nakamura N, Rabouille C, Watson R, Nilsson T, Hui N, Slusarewicz P, et al. Characterization of a cis-Golgi matrix protein, GM130. J Cell Biol 1995;131:1715-26.
31. Mu FT, Callaghan JM, Steele-Mortimer O, Stenmark H, Parton RG, Campbell PL, et al. EEA1, an early endosome-associated protein. EEA1 is a conserved alpha-helical peripheral membrane protein flanked by cysteine "fingers" and contains a calmodulin-binding IQ motif. J Biol Chem 1995;270:13503-11.
32. Steegmaier M, Yang B, Yoo JS, Huang B, Shen M, Yu S, et al. Three novel proteins of the syntaxin/SNAP-25 family. J Biol Chem 1998;273:34171-9.
33. Lundstrom A, Serre G, Haftek M, Egelrud T. Evidence for a role of corneodesmosin, a protein which may serve to modify desmosomes during cornification, in stratum corneum cell cohesion and desquamation. Arch Dermatol Res 1994;286:369-75.
34. Griffiths G, Simons K. The trans Golgi network: sorting at the exit site of the Golgi complex. Science 1986;234:438-43.
35. Rodriguez-Boulan E, Musch A. Protein sorting in the Golgi complex: shifting paradigms. Biochim Biophys Acta 2005;1744:455-64.
36. Ishida-Yamamoto A, Kishibe M. Involvement of corneodesmosome degradation and lamellar granule transportation in the desquamation process. Med Mol Morphol 2011;44:1-6.
37. Moniaga CS, Jeong SK, Egawa G, Nakajima S, Hara-Chikuma M, Jeon JE, et al. Protease activity enhances production of thymic stromal lymphopoietin and basophil accumulation in flaky tail mice. Am J Pathol 2013;182:841-51.
38. Oji V, Eckl KM, Aufenvenne K, Natebus M, Tarinski T, Ackermann K, et al. Loss of corneodesmosin leads to severe skin barrier defect, pruritus, and atopy: unraveling the peeling skin disease. Am J Hum Genet 2010;87:274-81.
39. Basel-Vanagaite L, Attia R, Ishida-Yamamoto A, Rainshtein L, Ben Amitai D, Lurie R, et al. Autosomal recessive ichthyosis with hypotrichosis caused by a mutation in ST14, encoding type II transmembrane serine protease matriptase. Am J Hum Genet 2007;80:467-77.
40. Chavanas S, Bodemer C, Rochat A, Hamel-Teillac D, Ali M, Irvine AD, et al. Mutations in SPINK5, encoding a serine protease inhibitor, cause Netherton syndrome. Nat Genet 2000;25:141-2.
41. Akiyama M, Sugiyama-Nakagiri Y, Sakai K, McMillan JR, Goto M, Arita K, et al. Mutations in lipid transporter ABCA12 in harlequin ichthyosis and functional recovery by corrective gene transfer. J Clin Invest 2005;115:1777-84.
42. Kelsell DP, Norgett EE, Unsworth H, Teh MT, Cullup T, Mein CA, et al. Mutations in ABCA12 underlie the severe congenital skin disease harlequin ichthyosis. Am J Hum Genet 2005;76:794-803.
43. Sprecher E, Ishida-Yamamoto A, Mizrahi-Koren M, Rapaport D, Goldsher D, Indelman M, et al. A mutation in SNAP29, coding for a SNARE protein involved in intracellular trafficking, causes a novel neurocutaneous syndrome characterized by cerebral dysgenesis, neuropathy, ichthyosis, and palmoplantar keratoderma. Am J Hum Genet 2005;77:242-51.

METHODS

DNA sequencing with the Next Generation DNA Sequencer

Genomic DNA from *Tmem79*$^{ma/ma}$, CBA, and C57BL/6 mice was obtained from the liver. The extracted genomic DNAs were sequenced by using the SureSelect Target Enrichment System (Agilent Technologies Japan), which targeted an 85.0- to 92.0-Mb region excluding repetitive sequences and the 80.0- to 85.0-Mb and 92.0- to 93.0-Mb exonic regions on mouse chromosome 3. The enriched DNA fragments were sequenced for 75-bp single-end reads with an Illumina Genome Analyzer II (Illumina), according to the manufacturer's instructions. The raw image files were processed with Illumina SCS2.8 software using the default parameters. The extracted DNA sequence reads were mapped to the mouse reference genome (mm19) by using bwa. SAMtools was used to call SNVs/indels for each mouse based on the following filter conditions: base quality of 20 or greater and sequence depth of 10 or greater for SNVs and base quality of 50 or greater and sequence depth of 10 or greater for indels. Then we removed the SNVs/indels found in both CBA and *Tmem79*$^{ma/ma}$ as SNVs/indels between C57BL/6 and CBA. Finally, all candidate mutations were evaluated manually, and the exonic mutations were identified with the IGV viewer.

Antibodies

Anti-CDSN mouse mAb (Abcam, Tokyo, Japan), anti-EEA1 mouse mAb (MBL, Nagoya, Japan), anti-GM130 mouse mAb (Abcam), anti-FLG rabbit antibody (Covance, Princeton, NJ), anti-KLK5 mouse mAb (R&D Systems, Minneapolis, Minn), anti-LEKTI mouse mAb (Santa Cruz Biotechnology, Dallas, Tex), anti-Lamp1 mouse mAb (Santa Cruz Biotechnology), anti-LOR rabbit mAb (Gene Tex, Taiwan), anti-SNAP29 mouse mAb (Sigma, Fukushima, Japan), and anti-TGN46 sheep polyclonal antibody (Abcam) were used as primary antibodies for immunostaining. Alexa Fluor 488 Goat Anti-mouse IgG, Alexa Fluor 488 Donkey Anti-sheep IgG, and Alexa Fluor 568 Goat Anti-rabbit IgG (Life Technologies, Tokyo, Japan) were used as secondary antibodies.

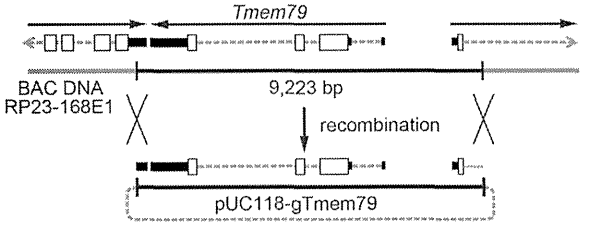

FIG E1. Transgene construct for *Tmem79* transgenic mice. Whole genomic regions, including Tmem79, and the 3′ untranslated region and exon 1 of adjacent genes were subcloned into pUC118 by using a Red/ET DNA recombination system and used to generate *Tmem79* transgenic mice.

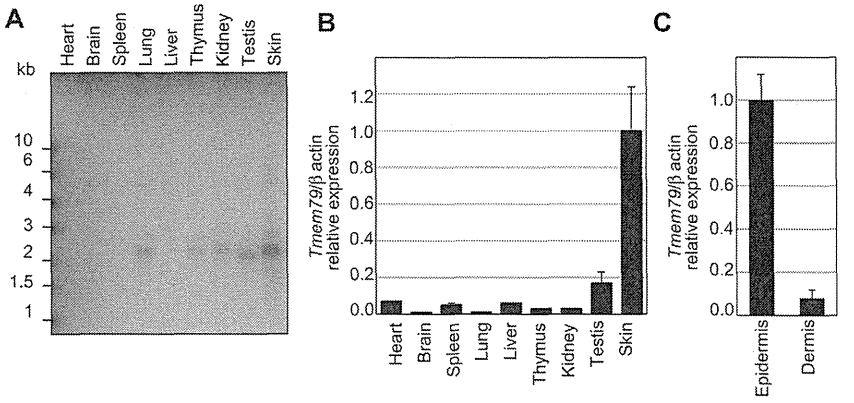

FIG E2. Transcription levels of *Tmem79* in various tissues. **A,** Northern blot analysis for *Tmem79* in various tissues in 8-week-old C57BL/6 mice. **B,** Quantitative PCR analysis for *Tmem79* in 8-week-old C57BL/6 mice. **C,** Quantitative PCR analysis for *Tmem79* in dermis and epidermis in 5-day-old C57BL/6 mice. These results indicate that *Tmem79* is mainly expressed in the epidermis of the skin.

TABLE E1. Difference of phenotype in flaky tail (*maFlg$^{ft/ft}$*), *Flg$^{-/-}$*, *Flg$^{ft/ft}$*, and *ma/ma* mice

	Flaky tail (*maFlg$^{ft/ft}$*)	*Flg$^{-/-}$*	*Flg$^{ft/ft}$*	*ma/ma*
Spontaneous dermatitis	+	−	−	+
Scratching behavior	+	−	−	+
Keratohyalin granules	−	−	−	+
TEWL	↑	→	→	↑
SC hydration	↓	→	→	↓

PLOS ONE

An Anilinoquinazoline Derivative Inhibits Tumor Growth through Interaction with hCAP-G2, a Subunit of Condensin II

Hirokazu Shiheido[1☯], Yuhei Naito[2☯], Hironobu Kimura[1], Hiroaki Genma[1], Hideaki Takashima[1], Mayuko Tokunaga[1], Takao Ono[3], Tatsuya Hirano[3], Wenlin Du[4], Taketo Yamada[4], Nobuhide Doi[1], Shiro Iijima[2], Yutaka Hattori[2], Hiroshi Yanagawa[1]*

1 Department of Biosciences and Informatics, Keio University, Kohoku-ku, Yokohama, Japan, **2** Clinical Physiology and Therapeutics, Faculty of Pharmacy, Keio University, Minato-ku, Tokyo, Japan, **3** Chromosome Dynamics Laboratory, RIKEN Advanced Science Institute, Wako, Saitama, Japan, **4** Department of Pathology, School of Medicine, Keio University, Shinjuku-ku, Tokyo, Japan

Abstract

We screened 46 novel anilinoquinazoline derivatives for activity to inhibit proliferation of a panel of human cancer cell lines. Among them, Q15 showed potent *in vitro* growth-inhibitory activity towards cancer cell lines derived from colorectal cancer, lung cancer and multiple myeloma. It also showed antitumor activity towards multiple myeloma KMS34 tumor xenografts in Icr/scid mice *in vivo*. Unlike the known anilinoquinazoline derivative gefitinib, Q15 did not inhibit cytokine-mediated intracellular tyrosine phosphorylation. Using our mRNA display technology, we identified hCAP-G2, a subunit of condensin II complex, which is regarded as a key player in mitotic chromosome condensation, as a Q15 binding partner. Immunofluorescence study indicated that Q15 compromises normal segregation of chromosomes, and therefore might induce apoptosis. Thus, our results indicate that hCAP-G2 is a novel therapeutic target for development of drugs active against currently intractable neoplasms.

Citation: Shiheido H, Naito Y, Kimura H, Genma H, Takashima H, et al. (2012) An Anilinoquinazoline Derivative Inhibits Tumor Growth through Interaction with hCAP-G2, a Subunit of Condensin II. PLoS ONE 7(9): e44889. doi:10.1371/journal.pone.0044889

Editor: Maria A. Deli, Biological Research Centre of the Hungarian Academy of Sciences, Hungary

Received February 28, 2012; **Accepted** August 15, 2012; **Published** September 13, 2012

Funding: This work was supported by grants for a basic research program (CREST) of the Japan Science and Technology Agency and a program for Promotion of Fundamental Studies in Health Sciences of the National Institute of Biomedical Innovation (NIBIO), Japan, as well as a Grant-in-Aid for Scientific Research (22310121) and a grant for Strategic Research Foundation Grant-aided Projects for Private Universities (S0801008 and S0901009) from Ministry of Education, Culture, Sport, Science, and Technology (MEXT), Japan. The funders had no role in study design, data collection or analysis, decision to publish, or preparation of the manuscript.

Competing Interests: The authors have declared that no competing interests exist.

* E-mail: hyana@bio.keio.ac.jp

☯ These authors contributed equally to this work.

Introduction

Although advances in treatment, such as combination chemotherapy and chemoradiation, have slightly improved the outcome of tumor therapy over the last several decades [1], tumors are the leading cause of death in economically developed countries and the second leading cause of death in developing countries [2]. Colorectal tumors, lung tumors, and multiple myeloma (a hematopoietic tumor) are particularly intractable. Therefore, novel drugs having potent activity are required to treat such tumors, and in order to develop them, it is important to identify novel molecular targets related to the pathogenesis of these intractable tumors.

Anilinoquinazoline derivatives such as gefitinib and erlotinib, selective tyrosine kinase inhibitors, have been reported to be effective against recurrent non-small-cell lung tumor [3,4]. Here, we screened 46 anilinoquinazoline derivatives, which are structurally similar to gefitinib or erlotinib, for growth-inhibitory activity towards a panel of intractable tumor cell lines. Among these compounds, we identified Q15 as a potent proliferation inhibitor and apoptosis inducer of the colon tumor, lung tumor and multiple myeloma cell lines examined. We further confirmed that Q15 showed higher antitumor activity than gefitinib towards multiple myeloma KMS34 tumor xenografts in Icr/scid mice *in*

Table 1. IC_{50} values (μM) of anilinoquinazoline derivatives for inhibiting proliferation of different human tumor cell lines.

Cell lines	Compounds		
	Q15	Q16	Q17
KMS11	5.1	13.5	10.1
KMS27	14.5	19.1	20.9
KMS34	1.1	5.8	6.1
KMM1	4.7	22.1	20.3
RPMI8662	2.3	22.4	6.1
SW480	2.0	6.4	17.4
HeLa	3.3	7.3	13.5

doi:10.1371/journal.pone.0044889.t001

vivo. Surprisingly, however, Q15 did not inhibit intracellular signaling or the phosphorylation status of ERK1/2, indicating that the mechanism of its antitumor effect is different from that of gefitinib. Therefore, we next focused on the possible mechanism of action of Q15.

Previously we have developed an mRNA display system named *in vitro* virus (IVV) [5–7], in which an *in vitro*-translated full-length protein (phenotype) is covalently attached to its encoding mRNA (genotype) through puromycin [8]. Here, we employed this mRNA display method to search for the target of Q15 for induction of apoptosis, and identified hCAP-G2, which is a subunit of condensin II [9,10], as a Q15 binding partner. We further confirmed that Q15 binds to the condensin II complex through direct interaction with hCAP-G2, and therefore may affect chromosomal segregation in mitosis, resulting in abnormal cell division and subsequent apoptosis. These results indicate that Q15 is a promising candidate drug for treatment of high-risk multiple myeloma. Further, hCAP-G2 appears to be a novel therapeutic target for development of drugs active against currently intractable neoplasms.

Results

Identification of a Potent Proliferation Inhibitor of Several Multiple Myeloma Cell Lines from a Library of Anilinoquinazoline Derivatives

We screened a compound library consisting of 46 anilinoquinazoline derivatives for activity to inhibit proliferation of various sorts of intractable tumor cell lines. Five multiple myeloma cell lines (KMS11, KMS27, KMS34, KMM1 and RPMI8662), SW480 cells and HeLa were treated with 0.5–50 μM of each compound for 72 h and their viability was examined by means of MTS assay (Table 1). Q15 (Fig. 1A) showed the highest cytotoxicity among the compounds examined towards the cell lines tested here. Next, we compared Q15 with gefitinib in a KMS34 cell proliferation assay (Fig. 1B). The results indicated that Q15 is 6 times more potent than gefitinib.

In order to see whether the mechanism of action of Q15 differs from that of gefitinib, we examined inhibition of phosphorylation of ERK1/2, which is a key growth transducer of tumor cells, by Q15 and gefitinib. A549 cells were treated with 5 μM Q15 or gefitinib for 24 h in the absence or presence of EGF, then subjected to immunoblot analysis. Gefitinib inhibited the phosphorylation of ERK1/2, but Q15 did not (Fig. 1C). Furthermore, Q15 did not inhibit the phosphorylation stimulated by FGF2, HGF, VEGF or IL-6 (data not shown). Thus, these results indicate that the mechanism of action of Q15 is different from that of

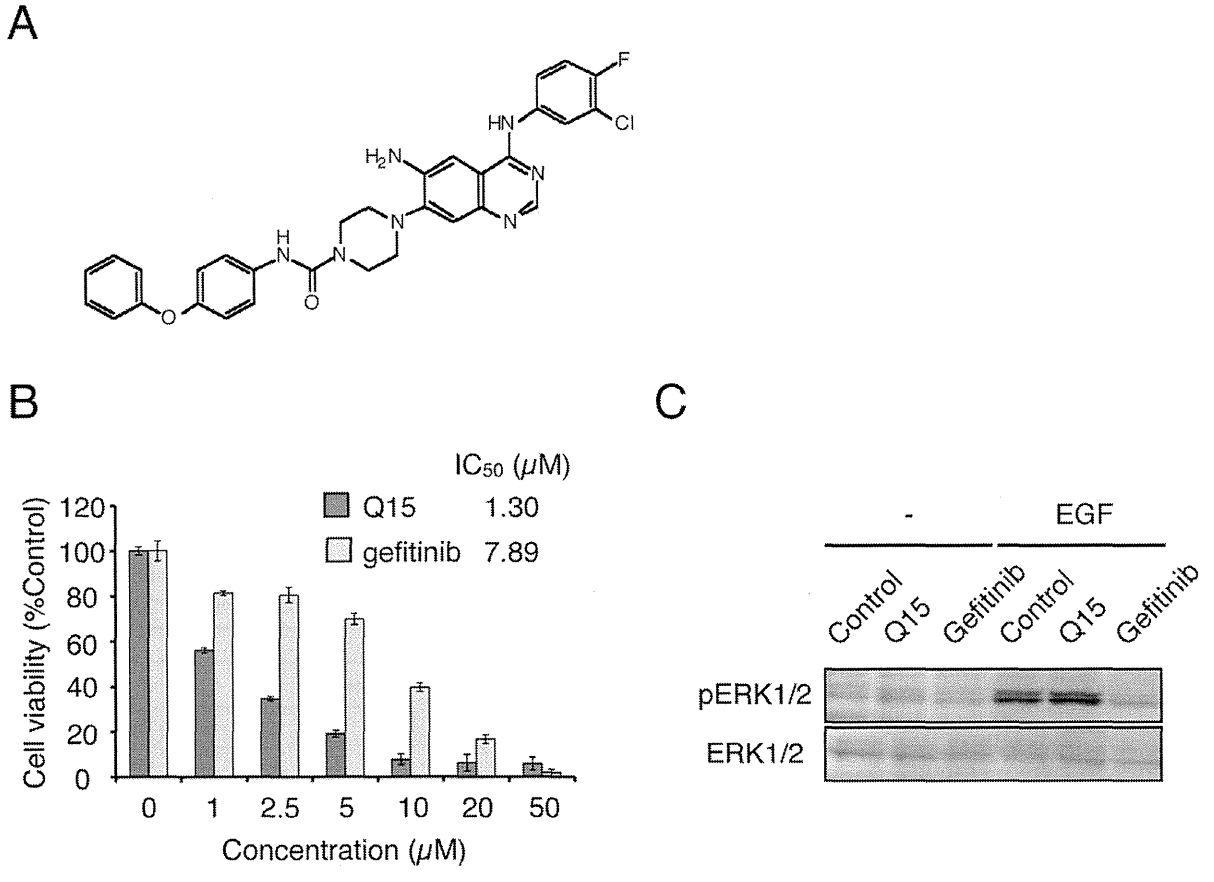

Figure 1. Q15 inhibits proliferation of tumor cells through a different mechanism from that of gefitinib. (A) Chemical structure of Q15. (B) KMS34 cells were incubated with 0–50 μM Q15 or gefitnib for 72 h. Then, cell viability was determined by means of MTS assay. (C) A549 cells were incubated with DMSO or 5 μM Q15 for 24 h in the absence or presence of 50 ng/mL EGF for 48 h. Whole cell lysates were analyzed by Western blotting with anti-pERK1/2 or anti-ERK1/2 antibody.
doi:10.1371/journal.pone.0044889.g001

Table 2. IC_{50} values (μM) of Q15 for inhibiting proliferation of different human tumor cell lines.

Cell Lines	IC_{50} (μM)	Cell Lines	IC_{50} (μM)
Breast cancer		Lung cancer	
HBC−4	2.2	NCI-H23	4.4
BSY-1	3.0	NCI-H226	3.1
HBC-5	3.1	NCI-H522	0.4
MCF-7	3.4	NCI-H460	1.7
MDA-MB-23	1.6	A549	1.3
Brain cancer		DMS273	1.3
U251	1.8	DMS114	1.7
SF-295	1.3	Kidney cancer	
SF-539	2.3	RXF-631L	1.8
SNB-75	1.6	Gastric cancer	
SNB-78	3.1	St-4	1.7
Colon cancer		MKN1	3.1
HCC2998	2.2	MKN7	1.6
HT-29	0.6	MKN28	2.7
HCT-15	1.7	MKN45	1.8
HCT-116	2.4	MKN74	1.4
Ovary cancer		Melanoma	
OVCAR-4	2.3	LOX-IMVI	0.4
SK-OV-3	2.9		

doi:10.1371/journal.pone.0044889.t002

gefitinib, despite the structural similarity between the two compounds.

We next tested the antitumor activity of Q15 against several human cancer cell lines, including breast, brain, colon, lung, ovary, kidney, gastric cancer and melanoma (Table 2). Q15 inhibited the growth of all the tumor cell lines examined, suggesting that it may have activity against a wide range of human cancers.

Q15 Inhibits Cell Proliferation of Multiple Myeloma and Induces Apoptosis Both *in vitro* and *in vivo*

We next examined the ability of Q15 to induce apoptosis of tumor cells. KMS34 cells were treated with 20 μM Q15 for 0–24 h and then immunoblot analysis of the whole cell lysates was performed. Activation of caspase-3 and 9, leading to cleavage of PARP, was detected (Fig. 2A). These results suggest that Q15 induces caspase-dependent apoptosis of tumor cells.

To examine whether Q15 exhibits antitumor activity *in vivo*, we performed *in vivo* tumor proliferation assay. KMS34 tumor xenografts were treated with intraperitoneal injection of 20 mg/kg of Q15 twice, with a three-day interval, and then the time-course of tumor volume was followed for 16 days (Fig. 2B and C). On the 16th day, Q15 achieved statistically significant inhibition of tumor growth ($P<0.02$). No significant change of body weight was observed in Q15-treated mice, suggesting that systemic toxicity of Q15 is likely low. In order to examine whether Q15 induces apoptosis of tumor cells *in vivo*, we also performed histopathological examination of tumor tissue. In Q15-treated mice, a number of tumor cells exhibited aggregation of chromatin, as compared with the control (Fig. 2D). This result indicates that Q15 induces apoptosis of tumor cells *in vivo*, as well as *in vitro*.

Identification of Q15-binding Protein using mRNA Display

To elucidate the mechanism through which Q15 inhibits proliferation of tumor cells, we set out to identify Q15-binding proteins by means of mRNA display [5–7], as illustrated in Fig. 3A. We prepared a cDNA library derived from total RNA of human colon carcinoma SW480 cells, because, like other tumor cells, SW480 cells were sensitive to Q15. Proteins that bind to Q15-Bio (Fig. 3B) immobilized on beads were selected using mRNA display. From the library obtained after 5 rounds of selection, we analyzed the DNA sequences of 100 clones. Among them, we obtained six clones of a fragment of the Luzp5/NCAPG2 gene encoding hCAP-$G2_{262–476}$ containing the HEAT (Huntingtin, elongation factor 3, a subunit of protein phosphatase 2A, TOR lipid kinase) repeat domain (Fig. 4A). Although three other clones were obtained redundantly, they were confirmed to be false-positive clones by means of binding assay (data not shown). hCAP-G2 is a subunit of condensin II complex, which is regarded as a key player in mitotic chromosome condensation [9,10,11].

To confirm the interaction between hCAP-G2 and Q15, we performed an *in vitro* binding assay. Whole cell lysates were prepared from SW480 and KMS34 cells and incubated with Q15-immobilized beads for 1 h, followed by immunoblot analyses with specific antibodies (Fig. 4B and C). We found that hCAP-G2 in the cell lysates from both SW480 and KMS34 interacted specifically with Q15-immobilized beads; no interaction with mock beads was detected. Further, we found that SMC2, another subunit of condensin II complex, was also retained specifically on the Q15-immobilized beads. The interaction between hCAP-G2 and Q15 was further investigated by means of a competitive binding assay. Binding of hCAP-G2 to Q15 was inhibited in the presence of 100 μM free Q15, indicating that hCAP-G2 interacts not with the biotin linker, but with Q15 itself (Fig. 4D). We also confirmed that *in vitro* translated-hCAP-$G2_{262–476}$ binds directly to Q15 (data not shown). These results suggest that Q15 binds to the condensin II complex through direct interaction with hCAP-G2 in cell lysates prepared from both SW480 and KMS34.

Q15 Compromises Mitotic Chromosome Segregation and Eventually Induces Apoptosis

Condensins contribute to chromosome assembly and segregation in mitosis [9,12,13]. Therefore, we carried out an immunofluorescence analysis to examine the effects of Q15 on the behavior of chromosomes. For this purpose, we selected HeLa cells, since they have a large nucleus and intranuclear structures can be easily observed, whereas KMS34 and SW480 cells are too small for convenient observation of intracellular or intranuclear components. After 24 h treatment with Q15, HeLa cells were labeled with antibodies against hCAP-G and hCAP-H2 to visualize the distribution of condensin I and condensin II, respectively (Fig. 5A). In the Q15-treated cells, we observed about 80% of roundish and swollen chromosomes in which the otherwise distinct localizations of condensin I and condensin II were somewhat obscured (Fig. 5B). The defect in chromosome morphology observed here was reminiscent of, if not identical to, that reported previously in cells depleted of hCAP-G2 [9].

To examine whether or how Q15 may affect cell cycle progression, we next performed immunofluorescence labeling of cells with an antibody against α-tubulin and CREST, an autoimmune antiserum that recognizes the kinetochore/centromere region. When HeLa cells were treated with Q15 at a final concentration of 10 μM, atrophy of the cytoplasm was observed during interphase (Fig. 6A). Moreover, the frequency of cells with

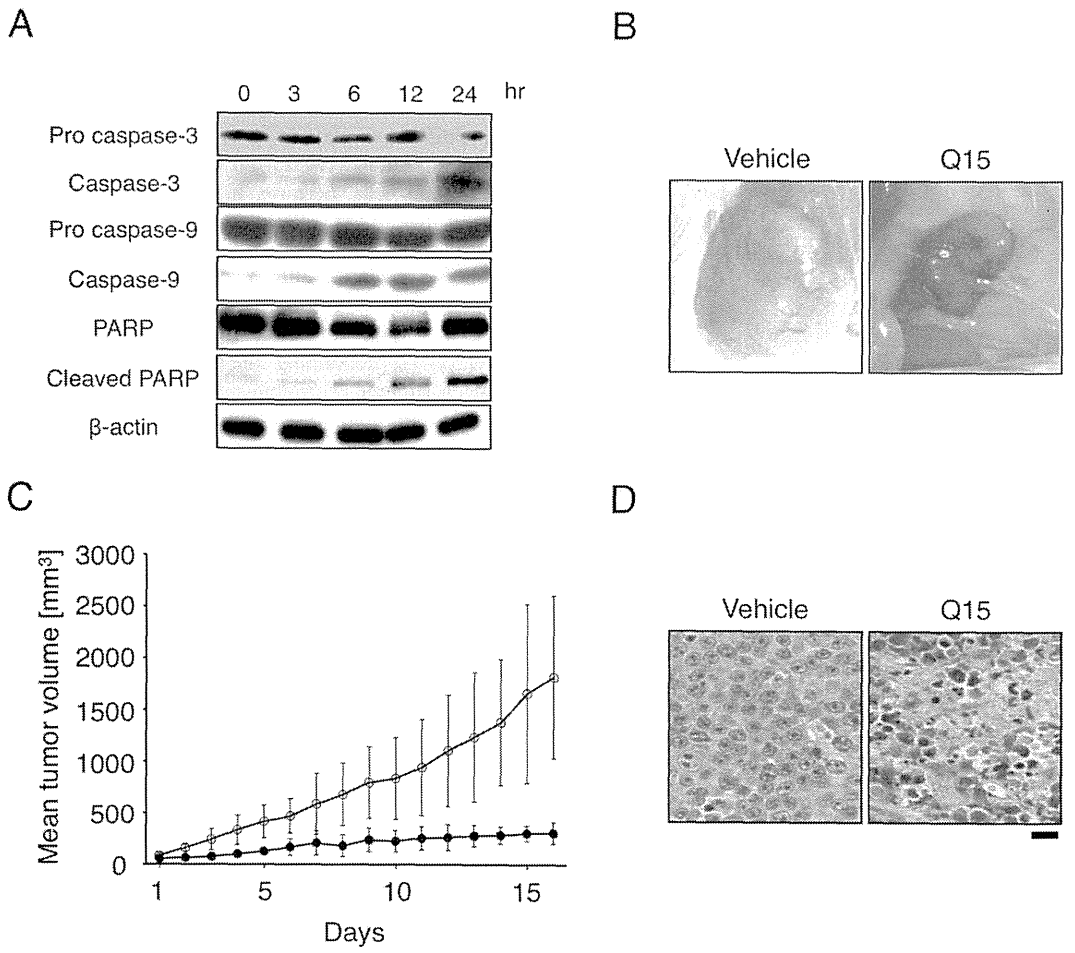

Figure 2. Q15 suppresses tumor growth and induces apoptosis of multiple myeloma cells *in vitro* and *in vivo*. (A) KMS34 cells were incubated with 20 μM Q15 for 0–24 h. The whole cell lysates were analyzed by immunoblot with anti-caspase-3, caspase-9, PARP or β-actin antibody, respectively. (B) KMS34 cells (3×10^7 cells) were inoculated subcutaneously into Icr/scid mice. Then, 20 mg/kg Q15 was injected intraperitoneally twice every 3 days. Representative tumor from each group. (C) The width and length of the plasmacytoma were measured and tumor volume was calculated. (D) Sections were stained with hematoxylin and eosin.
doi:10.1371/journal.pone.0044889.g002

defects in metaphase and anaphase was increased as compared with the control (Fig. 6B). In the metaphase population, more than 50% of mitotic cells showed defects in chromosome alignment (Fig. 6B, metaphase Incomplete). In the ana/telophase population, the frequency of cells with chromosomal bridging and lagging chromosomes among Q15-treated cells was about twice that in untreated cells. As shown in Fig. 6C, the most obvious defect was incompletely aligned chromosomes in metaphase. In these cells, poorly organized chromosomes were scattered and failed to be aligned properly on the metaphase plate. Again, this mitotic phenotype was reminiscent of that previously observed in cells depleted of condensin II [13]. Thus, these results indicate that Q15 compromises proper assembly and segregation of chromosomes, possibly by interfering with the function of condensin II.

We finally examined whether abnormal cell division induced by Q15 affects the nuclear structure of cells. KMS34 cells were treated with 5 μM Q15 for 24 h and observed with an electron microscope (Fig. 7). The Q15-treated cells showed segmented nuclei, while control cells had a single nucleus. These results suggest that interaction of Q15 with hCAP-G2 induces abnormal mitosis, resulting in multinucleated cells.

Discussion

In this study, we identified a novel anilinoquinazoline derivative Q15 as a potent inhibitor of proliferation of cancer cell lines derived from a variety of tissues. Our results also indicated that Q15 has a more potent antitumor activity than gefitinib, an anilinoquinazoline derivative that has a well-established antitumor effect on recurrent non-small-cell lung tumor [14]. However, unlike gefitnib, Q15 did not inhibit intracellular signaling or the phosphorylation status of ERK1/2, indicating that the mechanism of its antitumor effect is different from that of gefitinib.

We have developed mRNA display using IVV [7,15,16] as a simple and totally *in vitro* screening tool for protein-protein [15], protein-peptide [17–19], antigen-antibody [20,21], protein-DNA [22], protein-RNA [23] and protein-drug [24] interactions. In this mRNA display methodology, molecules that interact with target proteins are amplified by RT-PCR, and the amplified sequences are identified by DNA sequencing. Functional domains are easily extracted based on the identified sequences obtained from a randomly primed prey library as a non-biased representation [16,25]. Bait mRNA templates were prepared using an *in vitro* procedure that makes the previously employed *in vivo* IVV cloning steps unnecessary [7]. Because mRNA display using IVV is an

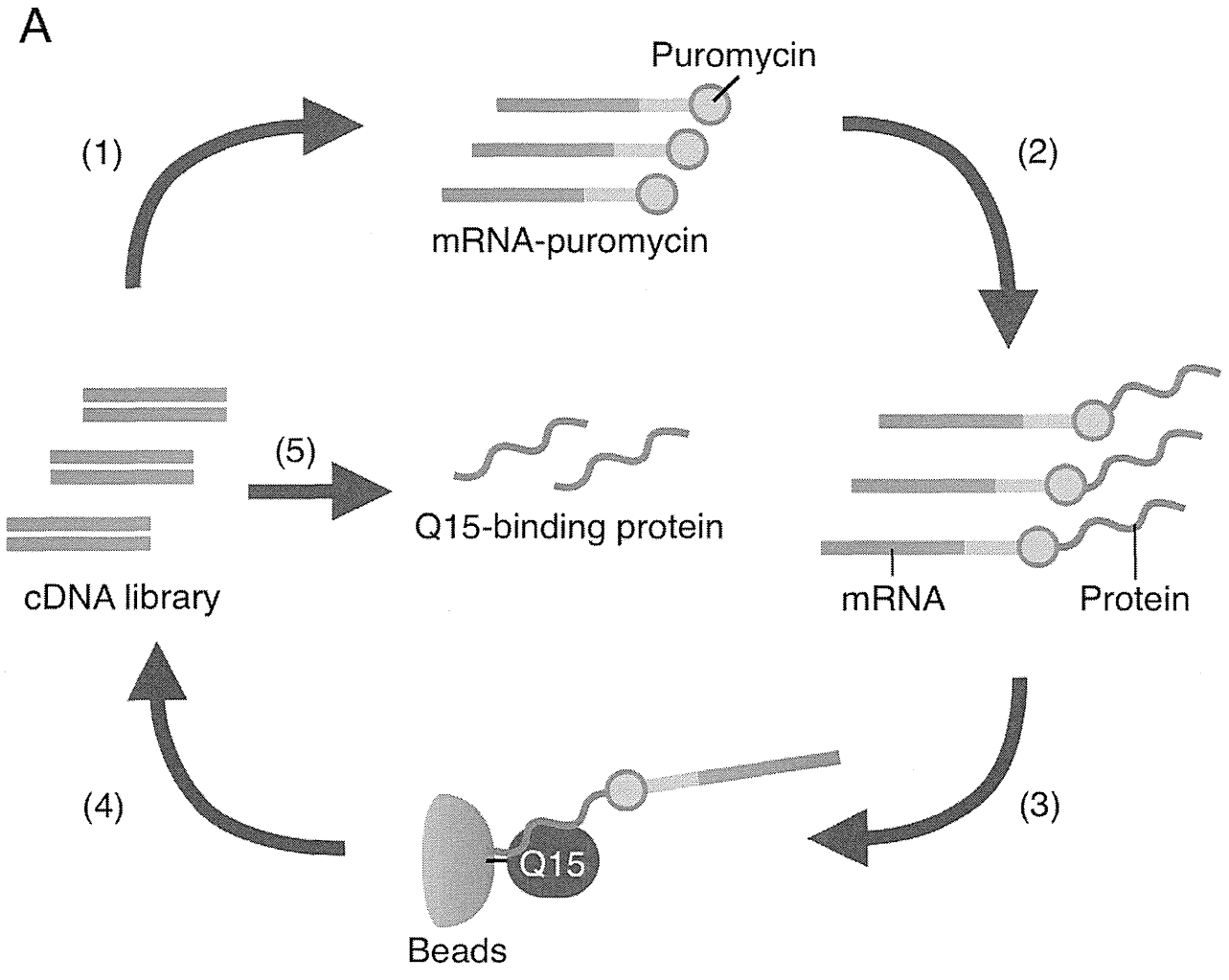

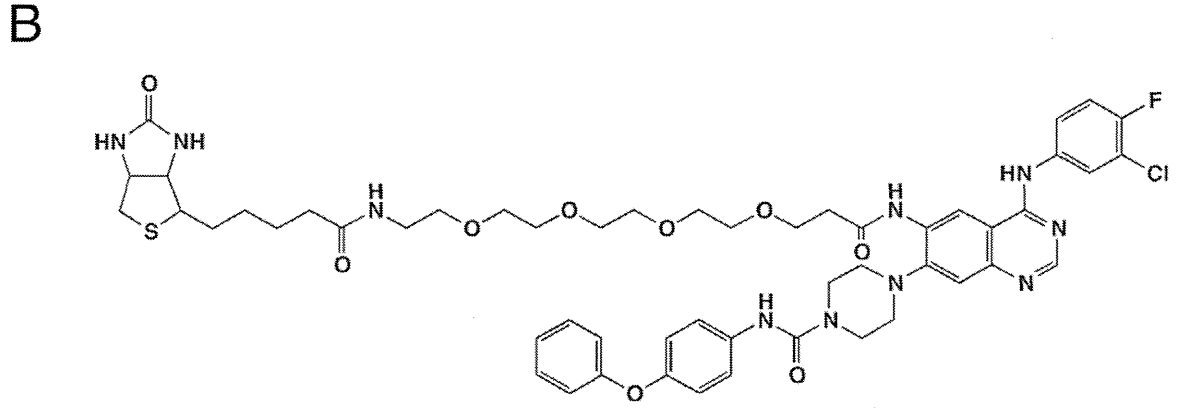

Figure 3. Schematic representation of in vitro selection of Q15-binding protein by mRNA display. (A) A cDNA library derived from SW480 cells was transcribed, ligated with PEG-Puro spacer (1) and translated in vitro (2) to form a protein-mRNA conjugates library. The library was incubated with biotinylated Q15-immobilized beads (3) and unbound molecules were washed away. The bound molecules were eluted and their mRNA portion was amplified by RT-PCR (4). The resulted DNA was used for the next round of selection and analyzed by cloning and sequencing (5). (B) The chemical structure of biotinylated Q15.
doi:10.1371/journal.pone.0044889.g003

entirely *in vitro* process, both toxic and nontoxic interacting proteins can be characterized. This is a distinct advantage of this method, because toxic proteins are not amenable to characterization by assays that require *in vivo* steps, such as Y2H [26] and TAP-MS [27].

Application of this approach here identified a HEAT-repeat domain of hCAP-G2, which is one of the subunits of condensin II

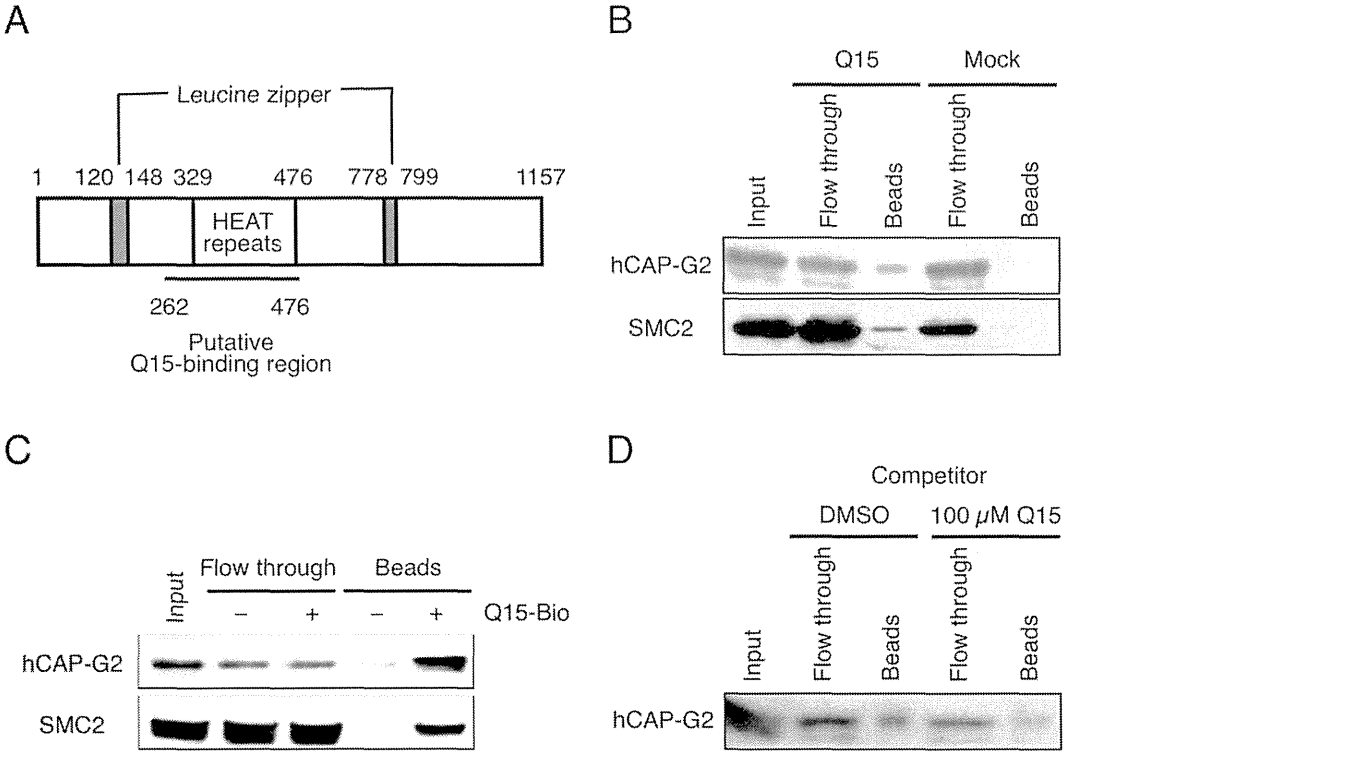

Figure 4. hCAP-G2 protein interacts directly with Q15. (A) Domain structure of hCAP-G2. The region (262–476) selected by mRNA display is underlined. (B and C) Lysates from KMS34 (B) and SW480 (C) cells were incubated with Q15-immobilized beads for 2 h. Each fraction was subjected to 10% SDS-PAGE. Protein bands were detected by immunoblotting with antibodies against hCAP-G2 and SMC2. (D) Cell lysates from KMS34 cells were incubated with Q15-immobilized beads for 2 h in the absence or presence of 100 μM free Q15. Each fraction was subjected to 10% SDS-PAGE and protein bands were detected by immunoblotting with antibodies against hCAP-G2.
doi:10.1371/journal.pone.0044889.g004

complex, as a Q15 binder that might be related to inhibition of cell proliferation. The condensin II complex is composed of SMC2 and SMC4 ATPases and three auxiliary subunits (hCAP-G2, hCAP-D3 and hCAP-H2) [9,10,14,28]. In binding assay using Q15-immobilized beads, SMC2 was co-precipitated with hCAP-G2, suggesting that Q15 interacts not with monomeric hCAP-G2, but with the holo-complex of condensin II. In condensin I, the HEAT-repeat domains of hCAP-G and hCAP-D2 are suggested to play important roles in their interaction with hCAP-H [29]. Therefore, this might also be the case for the interaction between hCAP-G2 and hCAP-H2. In fact, our data suggested that Q15 binds to HEAT repeats of hCAP-G2, which are thought to facilitate protein-protein interaction [11]. It is therefore possible that Q15 inhibits interactions between hCAP-G2 and hCAP-H2 or between hCAP-G2 and any other chromosomal proteins.

Previous studies showed that siRNA-mediated depletion of hCAP-G2 from HeLa cells results in severe defects in metaphase chromosome morphology [9], chromosome alignment and anaphase chromosome segregation [30]. Other studies also suggested that condensins regulate mitotic chromosome segregation in many different organisms [10,12,13]. Here, we have observed distortion of metaphase chromosome morphology, as well as incomplete alignment of metaphase chromosomes, in Q15-treated cells. These features are similar, if not identical, to the phenotypes observed in hCAP-G2-depleted cells, implying that binding of Q15 to hCAP-G2 inhibits condensin II function. Electron microscopic observations further indicated that abnormal cell division induced by Q15 resulted in formation of multinucleated cells.

In conclusion, we have identified a novel anilinoquinazoline derivative Q15 as a growth inhibitor of several intractable cancer cell lines. Using our mRNA display technology, we identified hCAP-G2, a subunit of condensin II complex, which is regarded as a key player in mitotic chromosome condensation, as a Q15 binding partner. We further showed that Q15 induces apoptosis and abnormal chromosome segregation during cell division. Taken together, our results indicate that Q15 may induce mitotic failure in tumor cells by interfering with condensin II function, and this leads to apoptosis. Therefore, inhibition of condensin function could be a novel strategy for the development of antitumor drugs for a range of tumors that are unresponsive to existing drugs.

Materials and Methods

Cell Lines

Multiple myeloma cell lines (KMM1, KMS11, KMS26, KMS27, KMS34 and RPMI8226) were generous gifts from Prof. T. Otsuki (Kawasaki Medical College, Kurashiki, Japan) [31] and were maintained in RPMI1640 medium with 10% fetal bovine serum and 1% penicillin/streptomycin. HeLa cells (RIKEN Cell Bank, 2002) and SW480 cells (ATCC, 2005) were maintained in DMEM with 10% fetal bovine serum and 1% penicillin/streptomycin. The sources of other human cancer cell lines are described elsewhere [32]. All cell lines were expanded immediately upon receipt, and multiple vials of low-passage cells were maintained in liquid N_2. No vial of cells was cultured for more than 3 months. The cells were tested routinely for Mycoplasma

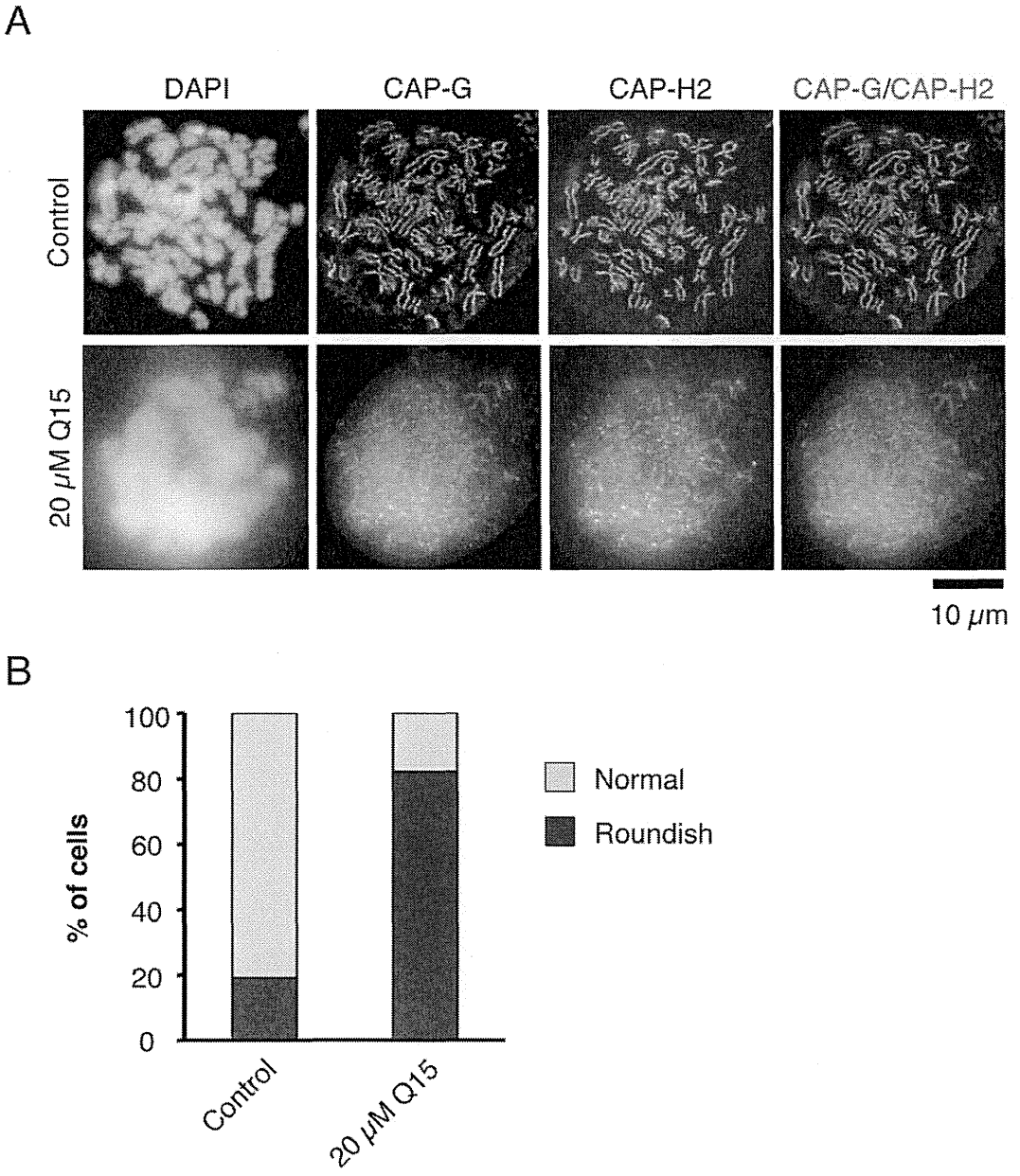

Figure 5. Q15 induces structural aberration of chromosomes in mitosis. (A) HeLa cells were treated with DMSO or 20 μM Q15 for 24 h. Then, immunofluorescence staining with antibodies against hCAP-G (green) and hCAP-H2 (red) was performed. DNA was stained with DAPI. Bar, 10 μm. (B) At least 100 cells were counted, and the percentages of normal and roundish cells were quantified.
doi:10.1371/journal.pone.0044889.g005

and purity. The identification of cell lines was performed based on an STR Multiplex method that uses 9 different loci: D5S818, D13S317, D7S820, D16S539, vWA, TH01, Amelogenin, TPOX and CSF1PO (Powerplex 1.2 system, Promega Corporation) in 2011.

Compounds

The syntheses of Q15 (6-amino-4(N)-(3-chloro-4-fluorophenyl)-7-[4-[4-phenoxy(phenylcarbamoyl)]piperazin-1-yl]quinazolin-4-amine) and biotinylated Q15 (Q15-Bio) are described in the Methods S1. All other anilinoquinazoline derivatives were synthesized from the corresponding quinazoline derivatives and aniline derivatives. The chemical structures of all synthetic compounds were confirmed by ^{1}H-NMR spectroscopy and mass spectrometry.

Cell Proliferation Assay

The cytotoxicity of each compound was assessed by MTS cell survival assays according to the instructions provided by the manufacturer (Promega, Madison, WI). Briefly, SW480 cells (1×10^{4} cells), KMS11, KMS21, KMS26, KMS28 or KMS34 cells (2.5×10^{4} cells, respectively) were plated in 96-well plates at a density of 20,000 cells per well. Synthetic anilinoquinazoline derivatives were dissolved in DMSO (Sigma) to make 20 mM stock solutions. The stock solutions were then diluted to 0.078–50 μM in medium and distributed in 96-well plates. After 48 or

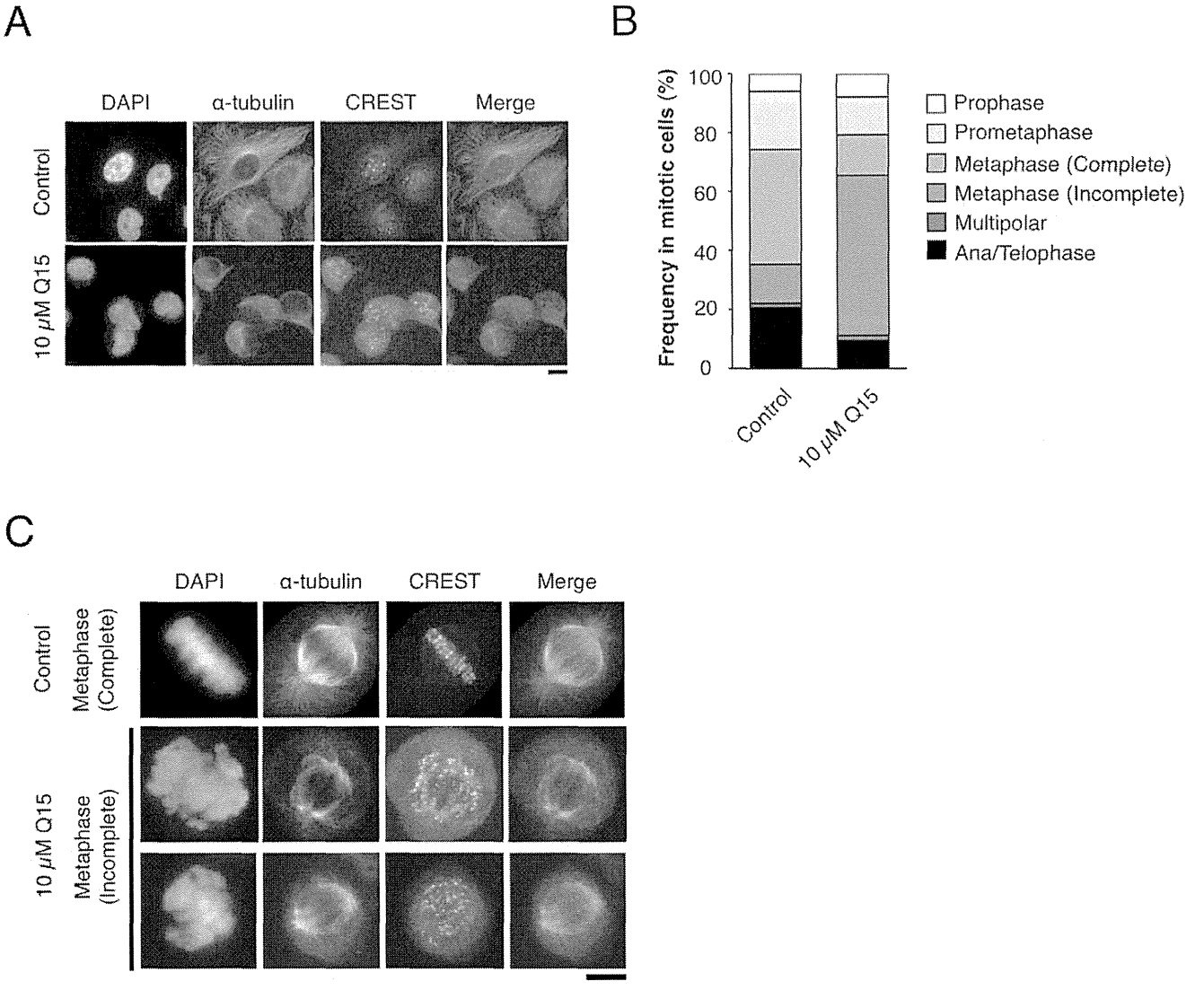

Figure 6. Q15 induces abnormal chromosome segregation. HeLa cells were treated with DMSO (Control) or 10 μM Q15 for 24 h, and immunofluorescence labeling with an antibody against α-tubulin (green) and CREST (red) was performed. DNA was stained with DAPI. (A) Representative images of interphase cells are shown. Bar, 10 μm. (B) Percentages of cells at different stages in mitotic populations are shown. The mitotic stages and alignment defects were judged by DAPI staining. (C) Representative metaphase cells are shown. Q15-treated cells display a dramatically high frequency of metaphase cells with incompletely aligned chromosomes. Bar, 10 μm.
doi:10.1371/journal.pone.0044889.g006

72 h treatment, 20 μL of the CellTiter 96 AQueous One Solution reagent (Promega) was directly added to each well and the plates were incubated at 37°C for 2 h in 5% CO_2 in air. The absorbance at 490 nm was read using a Safire^{TM} microplate reader (Tecan, Mannedorf, Switzerland).

Immunoblot Analysis

Cells were treated with 20 μM Q15 for 48 h followed by lysis in RIPA buffer (50 mM Tris pH 7.6, 150 mM NaCl, 1 mM EDTA, 0.5% sodium deoxycholate, 0.05% SDS, 1% NP-40) containing protease inhibitor cocktail (Nacalai Tesque, Kyoto, Japan). Protein concentrations were determined with a BCA protein assay kit (Thermo Scientific, Waltham, MA). Protein (20 μg) was run on 10 or 15% SDS-PAGE gel and analyzed with antibodies against caspase-9, caspase-3, PARP, p44/42 MAP kinase or phospho-p44/42 MAP kinase (all from Cell Signaling Technology, Beverly, MA). The blots were visualized with ECL chemiluminescence reagents (GE Healthcare, Waukesha, WI).

In vivo Tumor Growth Assay

Animal experiments were approved by the Ethics Committee for Animal Experiments at Keio University (no. 09118-0). *In vivo* tumor inhibition assay was performed as previously described [33] with several modifications. Briefly, 3×10^7 KMS34 cells were subcutaneously inoculated into 5-week-old male lcr/scid mice (CLEA, Tokyo, Japan). Plasmacytoma developed in 6 to 7 weeks, and when the size of the tumor had reached 50 mm^3 (day 1), vehicle (saline, 10% DMSO and 1% Tween 80) or 20 mg/kg of Q15 was injected intraperitoneally twice every 3 days. Tumor volumes was calculated according to the following formula: width×length^2×0.52 [33]. Differences in tumor size on day 14 were evaluated by means of Student's *t* test. $P<0.05$ was considered to indicate statistical significance.

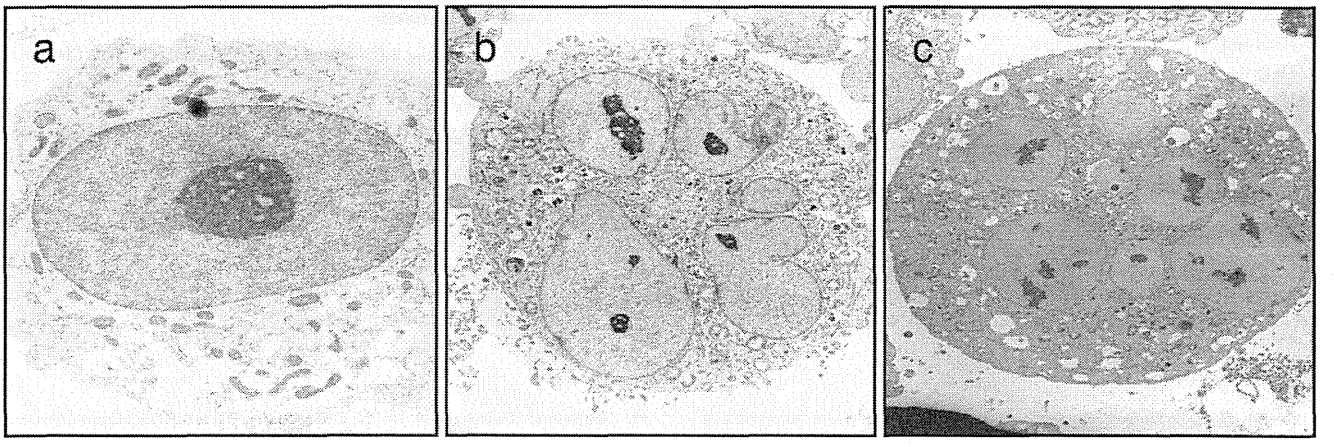

Figure 7. Q15 induces abnormal cell division. KMS34 cells were treated with DMSO (a) or 5 μM Q15 (b and c) for 24 h, then observed with an electron microscope. Micronuclei can be seen in Q15-treated cells.
doi:10.1371/journal.pone.0044889.g007

Histopathologic Examination

Histopathologic analysis was performed as previously described [33] with several modifications. When the size of subcutaneous tumors reached 50 mm^3, vehicle or 20 mg/kg Q15 was injected intraperitoneally twice every 3 days. After 14 days, the mice were killed and the tumors were isolated. Tumor samples were fixed with 10% formalin and embedded in paraffin. Sections were stained with hematoxylin and eosin.

mRNA Display Selection

Total RNA from SW480 cells was extracted with an RNeasy mini kit (Qiagen, Valencia, CA) and purified with a mTRAP mRNA isolation kit (Active Motif, Carlsbad, CA). A cDNA library was prepared as previously described [15]. The resulting cDNA library derived from KMS34 cells was transcribed using a RiboMAX large-scale RNA production system-SP6 (Promega) in a total volume of 20 μL containing 80 mM HEPES-KOH, pH 7.5, 2 mM spermidine, 40 mM DTT, 32 mM $MgCl_2$, 5 mM each of ATP, CTP, and UTP, 1 mM GTP, 5 mM $m^7G(5')ppp(5')G$ RNA capping analog (Invitrogen, Carlsbad, CA), 1 pmol of KMS34 cDNA library and SP6 RNA polymerase. The resulting RNA was purified with an RNeasy mini kit and ligated with a PEG-puromycin spacer [$p(dCp)_2$-T(fluorescent)p-PEGp-$(dCp)_2$-puromycin] [15] using T4 RNA ligase (Takara) for 15 h at 15°C in a total volume of 50 μL containing 50 mM Tris-HCl, pH 7.5, 10 mM $MgCl_2$, 12 mM DTT, 1.4 mM ATP, 5% DMSO, 0.002% BSA, 40 U of RNase inhibitor (Toyobo, Osaka, Japan), 0.2 mM PEG-puromycin spacer, 0.6 mM PEG2000 (Nacalai Tesque), 50 pmol of RNA, and 200 U of T4 RNA ligase. The resulting RNA-PEG-puromycin library was purified with the RNeasy mini kit. *In vitro* translation was performed in a total volume of 250 μL containing 25 pmol of the RNA-PEG-puromycin library, 50 μL of wheat germ cell-free extract (Zoegene, Kanagawa, Japan), 100 μg of creatine kinase, and 50 μL of a translation buffer (Zoegene) for 1 h at 26°C. The reaction mixture was added to Q15-Bio immobilized on Magnotex SA beads (Takara, Otsu, Japan) pre-equilibrated with IPP150 (10 mM Tris-HCl pH 8.0, 150 mM NaCl and 0.1% NP-40), and mixed on a rotator for 1 h at 4°C. The beads were washed five times with IPP150 and used as the template for RT-PCR with a OneStep RT-PCR kit (Qiagen) using primers (5′- GGAA-GATCTATTTAGGTGACACTATAGAACACAACAACAA-CAAACAACAACAAAAT-G-3′) and (5′-TTTTTTCTTGTCGTCATCGTCCTTGTAGTC-3′). The RT-PCR product was used for the next round of selection as described above. After five rounds of selection, the RT-PCR product was cloned using a PCR cloning kit (Qiagen) and sequenced with an ABI PRISM 3100 Genetic Analyzer (Applied Biosystems, Foster City, CA).

In vitro Binding Assay

SW480 or KMS34 cells were lysed with lysis buffer (50 mM Tris-HCl pH 7.5, 150 mM NaCl, 1% NP-40 and 0.1% DOC) containing protease inhibitor cocktail (Nacali tesque). The whole cell lysates were added to Q15-immobilized beads and mixed on a rotator for 1 h at 4°C in the absence or presence of 100 μM free Q15. The beads were washed five times with lysis buffer, followed by vortexing to elute the bound molecules. The resulting eluate was loaded on a 10% SDS-PAGE gel, and analyzed by immunoblot analysis with antibodies against LUZP5 (Bethyl Laboratories, Montgomery, TX) and SMC2 (Bethyl Laboratories).

Immunofluorescence Assay

HeLa cells on coverslips were treated with 5 μM Q15 for 24 h. Colcemid was then added at a final concentration of 0.02 μg/mL, and incubation was continued for another 3 h. Mitotic cells were collected by tapping the coverslips, followed by centrifugation at 1,000*g* for 5 min (Thermo/Shandon, Cyospin 4). The collected cells were fixed with 2% PFA in PBS at room temperature for 15 min, and treated with 0.5% Triton X-100 in PBS at room temperature for 5 min. The cells on coverslips were stained with an antibody against α-tubulin (Sigma, T9026/DM1A) and CREST [34], followed by Alexa488-labelled goat anti-mouse IgG and Alexa594-labelled goat anti-human IgG (Invitrogen, Carlsbad, CA). The mitotic spread cells were stained with antibodies against hCAP-G conjugated with biotin [30,35] and hCAP-H2 [9], followed by Alexa488-labelled streptavidin and Alexa594-labelled donkey anti-rabbit IgG (Invitrogen).

Electron Microscopic Observation

KMS34 cells were treated with 5 μM Q15 for 24 h. The cells were fixed in 2.5% glutaraldehyde in 100 mM sodium cacodylate (pH 7.2) for 1 h, washed, postfixed in 1% osmium tetroxide for 2 h, stained en bloc with uranyl acetate, dehydrated in a series of graded ethanol solutions, and embedded in an Epon/Araldite mixture. Ultrathin sections were stained with lead citrate and